

# Analysis of test beam data taken with a prototype of TPC with resistive Micromegas for the T2K Near Detector upgrade

D. Attié<sup>a</sup>, O. Ballester<sup>h</sup>, M. Batkiewicz-Kwasniak<sup>b</sup>, P. Billoir<sup>c</sup>,  
A. Blanchet<sup>c</sup>, A. Blondel<sup>c</sup>, S. Bolognesi<sup>a</sup>, R. Boullon<sup>a</sup>, D. Calvet<sup>a</sup>,  
M. P. Casado<sup>h,m</sup>, M.G. Catanesi<sup>d</sup>, M. Cicerchia<sup>e</sup>, G. Cogo<sup>f</sup>, P. Colas<sup>a</sup>,  
G. Collazuolf<sup>f</sup>, C. Dalmazzone<sup>c</sup>, T. Daret<sup>a</sup>, A. Delbart<sup>a</sup>, A. De Lorenzis<sup>h,1</sup>,  
S. Dolan<sup>n</sup>, K. Dygnarowicz<sup>i</sup>, J. Dumarchez<sup>c</sup>, S. Emery-Schrenk<sup>a</sup>,  
A. Ershova<sup>a</sup>, G. Eurin<sup>a</sup>, M. Feltre<sup>f</sup>, C. Forza<sup>f</sup>, L. Giannessi<sup>f</sup>, C. Giganti<sup>c</sup>,  
F. Gramegna<sup>e</sup>, M. Grassi<sup>f</sup>, M. Guigue<sup>c</sup>, P. Hamacher-Baumann<sup>g</sup>,  
S. Hassani<sup>a</sup>, D. Henaff<sup>a</sup>, F. Iacob<sup>f</sup>, C. Jesús-Valls<sup>h</sup>, S. Joshi<sup>a</sup>, R. Kurjata<sup>i</sup>,  
M. Lamoureux<sup>f</sup>, A. Langella<sup>k</sup>, J. F. Laporte<sup>a</sup>, L. Lavitola<sup>k</sup>, M. Lehuraux<sup>a</sup>,  
A. Longhin<sup>f</sup>, T. Lux<sup>h</sup>, L. Magaletti<sup>d</sup>, T. Marchi<sup>e</sup>, L. Mellet<sup>c</sup>, M. Mezzetto<sup>f</sup>,  
L. Munteanu<sup>n</sup>, Q. V. Nguyen<sup>c</sup>, Y. Orain<sup>c</sup>, M. Parif<sup>f</sup>, J.-M. Parraud<sup>c</sup>,  
C. Pastore<sup>d</sup>, A. Pepato<sup>f</sup>, E. Pierre<sup>c</sup>, C. Pio Garcia<sup>h</sup>, B. Popov<sup>c</sup>,  
J. Porthault<sup>a</sup>, H. Przybiliski<sup>b</sup>, F. Pupilli<sup>f</sup>, T. Radermacher<sup>g</sup>, E. Radicioni<sup>d</sup>,  
F. Rossi<sup>a</sup>, S. Roth<sup>g</sup>, S. Russo<sup>c</sup>, A. Rychter<sup>i</sup>, L. Scomparin<sup>f</sup>, D. Smyczek<sup>g</sup>,  
J. Steinmann<sup>g</sup>, S. Suvorov<sup>c</sup>, J. Swierblewski<sup>b</sup>, D. Terront<sup>c</sup>, N. Thamm<sup>g</sup>,  
F. Toussenel<sup>c</sup>, V. Valentino<sup>d</sup>, M. Varghese<sup>h</sup>, G. Vasseur<sup>a</sup>, U. Virginet<sup>c</sup>,  
U. Yevarouskaya<sup>c,1</sup>, M. Ziembicki<sup>i</sup>, M. Zito<sup>c</sup>

<sup>a</sup>IRFU, CEA, Université Paris-Saclay, Gif-sur-Yvette, France

<sup>b</sup>H. Niewodniczanski Institute of Nuclear Physics PAN, Cracow, Poland

<sup>c</sup>LPNHE, Sorbonne Université, CNRS/IN2P3, Paris, France

<sup>d</sup>INFN sezione di Bari, Università di Bari e Politecnico di Bari, Italy

<sup>e</sup>INFN: Laboratori Nazionali di Legnaro (LNL), Padova, Italy

<sup>f</sup>INFN Sezione di Padova and Università di Padova, Dipartimento di Fisica e  
Astronomia, Padova, Italy

<sup>g</sup>RWTH Aachen University, III. Physikalisches Institut, Aachen, Germany

<sup>h</sup>Institut de Física d'Altes Energies (IFAE) - The Barcelona Institute of Science and  
Technology (BIST), Campus UAB, 08193 Bellaterra (Barcelona), Spain

<sup>i</sup>Warsaw University of technology, Warsaw, Poland

<sup>j</sup>CERN, European Organization for Nuclear Research, Geneva, Switzerland

<sup>k</sup>INFN Sezione di Napoli and Università di Napoli Federico II, Dipartimento di Fisica,  
Napoli, Italy

---

\*Corresponding author

<sup>1</sup>uyevarou@lpnhe.in2p3.fr

## Abstract

In this paper we describe the performance of a prototype of the High Angle Time Projection Chambers (HA-TPCs) that are being produced for the Near Detector (ND280) upgrade of the T2K experiment. The two HA-TPCs of ND280 will be instrumented with eight Encapsulated Resistive Anode Micromegas (ERAM) on each endplate, thus constituting in total 32 ERAMs. This innovative technique allows the detection of the charge emitted by ionization electrons over several pads, improving the determination of the track position.

The TPC prototype has been equipped with the first ERAM module produced for T2K and with the HA-TPC readout electronics chain and it has been exposed to the DESY Test Beam in order to measure spatial and dE/dx resolution. In this paper we characterize the performances of the ERAM and, for the first time, we compare them with a newly developed simulation of the detector response.

Spatial resolution better than 800  $\mu\text{m}$  and dE/dx resolution better than 10% are observed for all the incident angles and for all the drift distances of interest. All the main features of the data are correctly reproduced by the simulation and these performances fully fulfill the requirements for the HA-TPCs of T2K.

*Keywords:* Resistive Micromegas, T2K Near Detector Time Projection Chambers

---

## Contents

|          |   |          |
|----------|---|----------|
| <b>1</b> | <b>Introduction and physics motivations</b>                     | <b>4</b> |
| <b>2</b> | <b>The ERAM technology and its use for the HA-TPC prototype</b> | <b>6</b> |
| <b>3</b> | <b>Experimental setup</b>                                       | <b>8</b> |

|           |  |           |
|-----------|--|-----------|
| 3.1       | HA-TPC field cage prototype . . . . .              | 8         |
| 3.2       | ERAM detector . . . . .                            | 10        |
| 3.3       | HA-TPC electronics . . . . .                       | 10        |
| <b>4</b>  | <b>Simulation of the ERAM response</b>             | <b>12</b> |
| 4.1       | Simulation framework . . . . .                     | 12        |
| 4.2       | Resistive layer simulation. . . . .                | 12        |
| <b>5</b>  | <b>Characterization of ERAM detector</b>           | <b>14</b> |
| <b>6</b>  | <b>Data collected at DESY</b>                      | <b>16</b> |
| <b>7</b>  | <b>Reconstruction and selection of tracks</b>      | <b>17</b> |
| <b>8</b>  | <b>ERAM response in data and simulation</b>        | <b>18</b> |
| <b>9</b>  | <b>Spatial resolution</b>                          | <b>20</b> |
| 9.1       | Spatial resolution for horizontal tracks . . . . . | 24        |
| 9.2       | Spatial resolution for inclined tracks . . . . .   | 25        |
| 9.3       | Biases in spatial resolution . . . . .             | 27        |
| <b>10</b> | <b>dE/dx resolution</b>                            | <b>29</b> |
| <b>11</b> | <b>Comparison between data and simulation</b>      | <b>32</b> |
| <b>12</b> | <b>E x B effect</b>                                | <b>33</b> |
| <b>13</b> | <b>Discussion and further improvements</b>         | <b>38</b> |
| <b>14</b> | <b>Conclusions</b>                                 | <b>40</b> |

## 1. Introduction and physics motivations

T2K is a long-baseline neutrino oscillation experiment that is taking data in Japan since 2010 [1]. By using an intense muon neutrino beam produced at the J-PARC accelerator complex and searching for the appearance of electron neutrinos at the far detector, Super-Kamiokande, T2K provided the first indications of  $\theta_{13}$  mixing angle being different from zero [1] followed by the first measurement of neutrino oscillations in appearance mode [2]. Recently first hints of Charge-Parity (CP) violation in the leptonic sector were also published by T2K [3].

In order to confirm these hints, T2K is now preparing the second phase of the experiment, that includes an upgrade of the neutrino beamline [4] and of the off-axis Near Detector complex, ND280 [5].

ND280 is a magnetized multi-purpose detector with several sub-detectors installed inside the UA1/NOMAD magnet that provides a magnetic field of 0.2 T. The core of ND280 is a tracker system, composed by two Fine Grained Detectors (FGDs) [6] and three Time Projection Chambers (TPCs) [7] instrumented with Bulk Micromegas modules [8]. The TPCs are used to track charged particles emitted in neutrino interactions and to measure their charge and momentum as well as to perform particle identification based on the ionization energy losses in the gas. The ND280 has been extensively used in all T2K oscillation analyses and it allows a reduction of systematic uncertainties to the level of 4–5% [9]. These uncertainties mostly come from our limited knowledge of neutrinos interactions with nuclei, and of the neutrino beam properties (energy spectrum and composition).

An upgrade of ND280 is being constructed [10], with the goal of further reducing these systematic uncertainties [11]. It consists in replacing one of the ND280 sub-detectors, the POD, with a new tracker system composed by a 3-dimensional scintillator target (Super-FGD) [12], made of  $\sim 2$  millions of  $1 \text{ cm}^3$  scintillator cubes each readout by three wavelength shifting fibers, two High Angle TPCs (HA-TPCs) and six Time-Of-Flight (TOF) planes [13]. Among other improvements, this upgrade, that will be installed at J-PARC in 2023, is expected to have a better efficiency to reconstruct high angle and backward-going tracks (with respect to the incoming neutrino direction) emitted in neutrino or antineutrino interactions thanks to the presence of the HA-TPCs. As for the already existing ND280 TPCs [7], the main goals of the two new HA-TPCs are the charged track reconstruction (to measure particle momentum) and the particle identification. This requires a good

spatial resolution on the reconstructed tracks and a precise ionization energy loss measurement.

Each endplate of the HA-TPC will be instrumented with 8 Encapsulated Resistive Anode Micromegas (ERAM). The first ERAM detector produced for ND280-Upgrade was initially tested using an X-ray test bench at CERN and then mounted on a prototype of the field cages that are being constructed for the HA-TPCs. This field cage prototype has the same construction materials, the same drift length and the same strip foils configuration to produce a uniform electric field as the cages that are being constructed for the ND280 Upgrade. Also, the final front-end electronics chain that will be used for the HA-TPCs, including two Front-End-Cards (FEC) each hosting eight AFTER chips [14], and one Front-End-Mezzanine (FEM) both equipped with their cooling plates, was mounted on the field cage. The FEM was connected to a Trigger and Data Concentrator Module (TDCM) [15] used for the data transfer to a DAQ computer via a MIDAS [16] front-end.

The TPC prototype was placed at the DESY T24/1 facility [17] inside a large-bore superconducting solenoid, called PCMAG, that provides a magnetic field of up to 1.25 T and it was exposed to an electron beam with momenta between 1 and 4 GeV/c. As we will show in this paper, this test beam campaign allowed to validate the performances of the TPCs for tracks with different incident angles with respect to the ERAM detector and for all the drift distances of interest for the T2K TPCs. With respect to the results presented in [18], the ERAM performances are also compared with a simulation that has been developed by using the ND280 software, adding the HA-TPCs ERAM geometry and the features of the resistive layers and of the AFTER chip electronics response.

This paper uses similar methods as those described in Refs. [18, 19] to analyze the test beam data, and the new results are consistent with the previously published ones. Some main changes should also be stressed:

- The field cage of the TPC prototype uses the same materials as the future HA-TPC and moreover, the maximal drift distance ( $\sim 1$  m) is much larger than the short drift distance of previous prototypes.
- The readout electronics is the same as the one of the final HA-TPC, and the response of the electronics has been studied and understood accurately.
- A Monte-Carlo simulation of ERAM response is now available and

agrees well with the data. This is new compared to previous analyses based only on data. This simulation is crucial as a tool to validate our understanding of the detector. It will be also crucial for future physics analysis with the upgraded ND280.

As it will be shown in the rest of this paper, the ERAM detector allows to reach an excellent spatial resolution, below 800  $\mu\text{m}$  for all the incident angles and drift distances, and an excellent  $dE/dx$  resolution, below 10% for tracks crossing the entire ERAM module. These performances are in good agreement with the ones predicted by the simulation that is able to reproduce both, low level variables, such as the charge sharing between neighboring pads or their time difference, as well as the spatial and the  $dE/dx$  resolution.

The paper is organized as follows. Section 2 introduces the ERAM technology and its use for the HA-TPC prototype. Section 3 presents the experimental setup. The simulation of the ERAM response is described in Section 4. Section 5 is devoted to the characterization of the ERAM detector. The data collected during the DESY test beam are presented in Section 6, while Section 7 provides a description of reconstruction algorithms. Section 8 is devoted to a comparison of ERAM response between data and simulation. Spatial and  $dE/dx$  resolutions are presented in Sections 9 and 10, respectively, while Section 11 discusses a comparison between the data and the simulation. A study of the  $E \times B$  effect is presented in Section 12. A short discussion on further potential improvements is given in Section 13. The conclusions in Section 14 close the paper.

## **2. The ERAM technology and its use for the HA-TPC prototype**

The ERAM technology, initially developed for the ILC prototypes [20], allows the detection of the charge induced by ionization electron on one pad (“leading pad”) over several adjacent or “neighbour” pads; this induced charge signal as a function of time or “waveform” that can be predicted. Combining the information from these signals on different pads forming a “cluster”, allows us to improve the spatial resolution, and hence the determination of the momentum of charge particles. Different ERAM prototypes have been tested at CERN [19] and at DESY [18] to characterize the ERAM response at short drift distances for tracks parallel to the ERAM detector plane, but with different angles compared to the pads borders. Tracks parallel (resp. inclined) to the horizontal borders of the pads are called “horizontal

tracks” (resp. “inclined tracks”) throughout this paper. Fig. 1 illustrates some typical waveform signals on pads of a cluster transverse to a horizontal track.

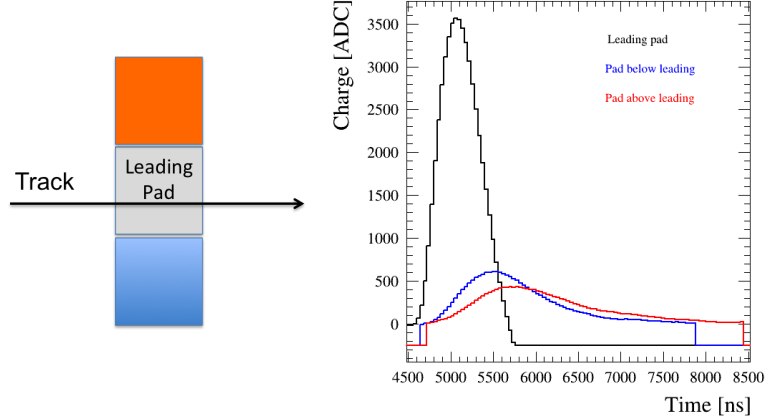


Figure 1: A schematic view of a column cluster (left) and the waveforms of each pad composing this cluster (right) for 412 ns shaping time of the electronics.

In the analyses of previous test beams at CERN [19] and at DESY [18], as well as in this paper, similar methods are used to reconstruct tracks. They are based on the maximal amplitudes of the waveforms in the pads of the clusters. Clusters of pads are defined as aligned transverse to horizontal tracks as in Fig. 1, or according to different and more precise topologies for inclined tracks. Each cluster allows to reconstruct a point or a “hit” of a track. A spatial resolution refers to the average accuracy of the position of one hit along a track. Studies are underway aiming at using simultaneously the full information of the waveforms of all the pads around the tracks in a global fit, to improve the track reconstruction accuracy. But a more simple approach is a robust reference for further studies, and can already show that the detector performances meet the physics requirements of the experiment. The results of these test beams allowed to validate the ERAM design and start the production of the 32 ERAMs that will be used to instrument the HA-TPCs.

The large drift distance available in the TPC prototype under tests, which is similar to the one of the final HA-TPC, is crucial to test our understanding of two important effects impacting the measured signals from the ERAM:

- The diffusion in the gas in the direction transverse to the track leads to what we call "charge sharing". Also, the initial ionization in the gas can lead to several avalanches reaching the same pad. This is a relatively simple statistical effect resulting in an effective "width" of the track, and increasing with the drift distance. The "sharing" of the charge with adjacent pads depends on this width and on the distance of the projected track in the ERAM plane, to the borders of the pads.
- The charge induced on pads adjacent to the "leading pad" due to the resistive effect is called "charge spreading" throughout this paper, though it is a more complex phenomenon than the charge sharing between pads resulting from the diffusion in the gas during the drift. They are correlations between the signals from pads of a cluster, and the signals in neighbour pads are delayed compared to the one of the leading pad, as shown in Fig. 1. This is different from the charge sharing effect from the diffusion in the gas, which is fixed at the time the charge reaches the ERAM detector.

The impact of these effects will be discussed after a detailed presentation of the obtained results.

### 3. Experimental setup

#### 3.1. HA-TPC field cage prototype

One of the main innovations of the HA-TPCs with respect to the vertical TPCs [7] currently used in ND280 is that the new field cage will use a single layer of solid insulator laminated on composite material, while for the current ND280 TPCs, two gas-tight boxes, one inside the other, are used. This new design minimizes the dead space and maximizes the tracking volume by reducing the distance between the outer TPC wall and the active gas volume from 12 cm to 4 cm. The radiation length of the material composing the field cage is 2%.

In order to test the construction process of the HA-TPCs field cages, several prototypes have been produced. One of them, that shares all the characteristics of the final field cages, was used for the test beam described in this paper.

The field cage prototype is built with lightweight and low-Z mechanical structures with a hollow shell shape constituting the box. The box is

laminated on an Aluminum mold in several layers, namely Kapton<sup>®</sup> sheets, aramide fiber-fabrics peels and honeycomb spacer panels glued together. The field cage is then enclosed on two sides with a cathode plane and the anode where the ERAM detector is located.

The innermost cage wall surface embeds a double layer of thin copper strips: the field strips for degrading the potential from the cathode to the anode and the mirror strips on the opposite side, for regularizing the field nearby the walls and for mitigating the effects of free charge deposition on dielectric surfaces. The strip foils are produced by the CERN Micro-Pattern Technologies service. In order to protect the field cage from the possible presence of tiny carbon fibers embedded into the aramide fiber fabric (Twaron) the mirror strip side is protected with an additional Kapton<sup>®</sup> coverlay glued on it.

The prototype has the same drift length (97.25 cm) as the HA-TPCs and a reduced transverse area ( $0.42 \times 0.42$  m) suitable to host one ERAM module. It was produced by the NEXUS company (Barcelona, Spain) and the different phases of the production of the prototype are shown in Fig. 2.

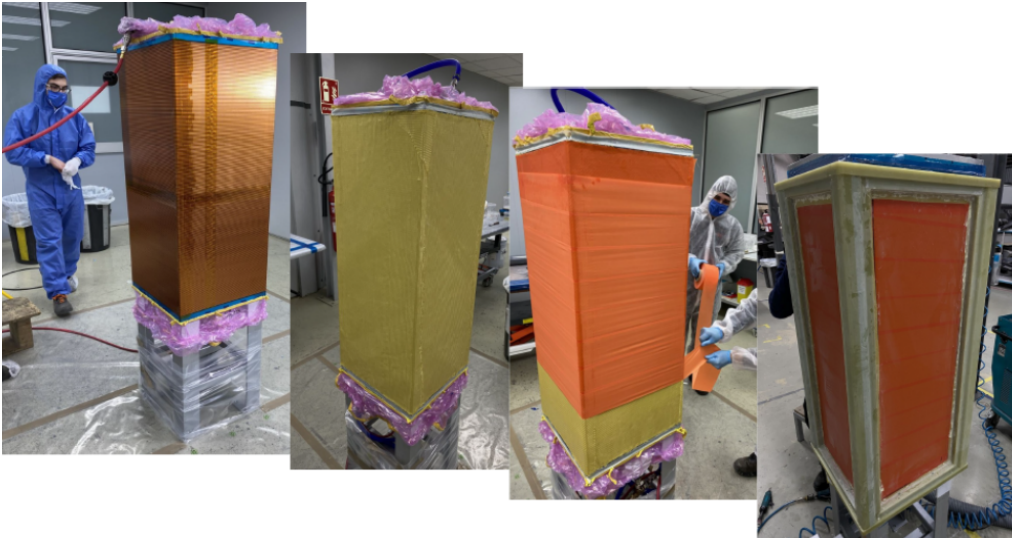


Figure 2: Phases of a field cage prototype production. From left to right: strip foil wrapped onto the mold, aramid fiber fabric (Twaron) glued onto the strip foil layer, Kapton<sup>®</sup> tape wrapped on the Twaron layer before glue curing phase, top and bottom flanges and angular bars applied. The vertical direction in these photos represents the drift direction and the ERAM will be installed on the top surface with the cathode on the bottom.

Prior to exposing the prototype to the electron beam at DESY, an extensive characterization of the field cage has been done at CERN. The properties were extremely good concerning fiberglass flanges smoothness quality, gas tightness (measured leakage below 0.1 l/h), inner surface quality and deformations smaller than 0.2 mm, compatible with prototype mold tolerances. We also performed several measurements of resistance and capacitance on the field and mirror strips showing that the electric field is behaving as expected.

### 3.2. ERAM detector

A description of the ERAM technology and of the detector used for the HA-TPCs of T2K is given in [18]. The ERAM modules built for T2K have a size of  $340 \times 420 \text{ mm}^2$  and are segmented in  $32 \times 36$  rectangular pads of size  $11.18 \times 10.09 \text{ mm}^2$ .

The ERAMs are used to readout the ionization electrons produced by charged particles crossing the TPC gas volume. These electrons are drifted to the anode readout plane of the TPC under a uniform electric field. On the readout plane, an avalanche is generated by a high electric field in the ERAM amplification region. The resulting pattern of illuminated pads corresponds to the trajectory of the track.

The main difference between the bulk-Micromegas technology used for the existing ND280 TPCs and an ERAM is that, in the case of bulk-Micromegas and for short drift distances the position reconstruction is limited by the pad size that is large compared to the size of the avalanche which falls on a metallic anode. In the ERAM, instead, the anode is covered by a foil of insulating material with a thin resistive layer on top, inducing signals over several pads. This allows a better reconstruction of the position of the charged particles crossing the TPC.

The ERAM detector uses a Diamond-Like Carbon (DLC) thin layer sputtered on a  $50 \text{ }\mu\text{m}$  thick APICAL<sup>®</sup> (Kapton<sup>®</sup>) insulator sheet. The detector installed on the field cage, named ERAM-01, has a resistivity of 300–400 kOhm/ $\square$  using DLC foils stack on a  $150 \text{ }\mu\text{m}$  glue layer.

### 3.3. HA-TPC electronics

The full electronics chain that will be used for the HA-TPCs has been installed on the ERAM-01 and tested during the test beam described in this paper. One of the goals of the test beam campaign was to validate the HA-TPC front-end electronics performance when placed inside a 0.2 T magnetic field. It has been then proved that their behavior is not altered.



Figure 3: Photo of one FEC with the 8 AFTER chips (left), and of one FEM (center). The right picture illustrates the final assembly of the ERAM with two FEC boards connected to one FEM; all electronic boards are equipped with their cooling plates.

The HA-TPC electronics, the main components are shown in Fig. 3, is based on the use of the AFTER chips [14], that had been designed for the existing ND280 TPCs. The AFTER chip is a 72-channel ASIC that includes preamplifiers and shapers with programmable gain and peaking time coupled to a 511-time bucket switched capacitor array (SCA). During the test beam the electronics peaking time was set to 200 or 412 ns.

The Front-End Cards (FEC) have been newly designed and host 8 AFTER chips. They are installed parallel to the ERAM modules and two FECs are used to readout one ERAM (1152 channels). The response linearity of the FEC has been measured with a dedicated campaign and showed a uniform response of all the channels with typical differences in linearity among neighboring pads smaller than 2%. The two FECs on each ERAM are connected to a Front-End Mezzanine (FEM) card that performs their control, synchronization and data aggregation. All connections, firstly between ERAM and FEC boards, secondly between FEC and FEM boards, are performed by using "floating" type connectors (HIROSE - FX23/FX23L series) in order to eliminate wired connections and all their drawbacks. The final production of electronic boards - both FECs and FEMs - was performed by the OUESTRONIC company in Rennes, France [21].

As back-end electronics we used the TDCM, a generic clock, trigger distributor and data aggregator module [15] designed for several projects, including the HA-TPCs. The collected data are transferred to a DAQ computer via a MIDAS [16] front-end and stored on disk for further analysis.

## 4. Simulation of the ERAM response

In this paper we are presenting the first comparisons between the data and a Monte Carlo simulation of the ERAM detector. To develop the simulation we benefited from the already extensively verified simulation of the T2K TPCs in the ND280 software [1]. The new feature that was implemented in the model for this work is the resistive layer of the ERAM detectors.

### 4.1. Simulation framework

The simulation starts from GEANT4 [22] that takes care of simulating the propagation of the charged particles in the TPC gas. To evaluate the energy loss and the produced ionization the PAI model [23] is used with at most a 1 mm computation step. The gas composition is the standard T2K gas [24], a mixture of Ar:CF<sub>4</sub>:iC<sub>4</sub>H<sub>10</sub> (95:3:2).

The primary energy deposition by a charged particle is converted into ionization electrons (typically 100 electrons per cm). The ionization potential for T2K gas is set to 26.8 eV. These electrons are moved to the ERAM plane with the arrival time estimated based on the drift velocity. The electrons are distributed on the sensitive plane following a Gaussian distribution assuming a transverse diffusion of  $\sigma_{trans} = 286 \mu\text{m}/\sqrt{\text{cm}}$  and a longitudinal diffusion of  $\sigma_{long} = 210 \mu\text{m}/\sqrt{\text{cm}}$ .

For each electron arriving to the ERAM the amplification is simulated based on the ERAM gain  $G$ . Fluctuations in the avalanche processes are taken into account by extracting the gain  $g_e$  for each electron as  $g_e = -\log(1 - \text{uniform}(0, 1)) \times G$ .

The amplified signal is then given as input to the simulation of the resistive layer that will be introduced in the next section. The resulting signal in each pad is then convoluted with the AFTER chip electronics response function and digitized with a sampling time of 40 ns.

### 4.2. Resistive layer simulation.

The behavior of the resistive layer can be approximated to a RC continuous network [25]. In this model, the charge density caused by the point-like electron deposited in  $\vec{r}_0 = (x_0, y_0)$  ( $\rho(\vec{r}, t = 0) = \delta_{\vec{r}_0}(\vec{r})$ ) is described with the solution of the 2D diffusion equation:

$$\rho(\vec{r}, t) = \frac{RC}{4\pi t} \times \exp\left(-\frac{r^2 RC}{4t}\right) \quad (1)$$

where  $r = \sqrt{(x - x_0)^2 + (y - y_0)^2}$  is a distance from the initial charge deposition,  $t$  is time and  $RC$  is a network characteristic of the ERAM. For our case, ERAM is expected to have an  $RC$  within 50-120 ns/mm<sup>2</sup>. To compute the observed charge in a given pad the equation above should be integrated over the pad surface

$$\begin{aligned}
Q_{unit}(t) &= \int_{x_{min}}^{x_{max}} \int_{y_{min}}^{y_{max}} \rho(\vec{r}, t) dx dy \\
&= \frac{1}{2}\pi \left( \text{Erf} \left[ \frac{\sqrt{RC}(x_{max} - x_0)}{2\sqrt{t}} \right] - \text{Erf} \left[ \frac{\sqrt{RC}(x_{min} - x_0)}{2\sqrt{t}} \right] \right) \\
&\quad \times \left( \text{Erf} \left[ \frac{\sqrt{RC}(y_{max} - y_0)}{2\sqrt{t}} \right] - \text{Erf} \left[ \frac{\sqrt{RC}(y_{min} - y_0)}{2\sqrt{t}} \right] \right)
\end{aligned} \tag{2}$$

where Erf is the error function and  $x_{min}$ ,  $x_{max}$ ,  $y_{min}$ ,  $y_{max}$  are pad borders coordinates.

The evolution of the charge in the pad is convoluted with the derivative of the AFTER electronics response:

$$E(t) = \left( \frac{t}{t_p} \right)^3 \exp \left( -\frac{3t}{t_p} \right) \sin \left( \frac{t}{t_p} \right) \tag{3}$$

where  $t_p$  is the electronics peaking time. The unit waveform ( $WF_{unit}$ ) is then:

$$WF_{unit}(t) = Q_{pad}(t) \otimes \frac{dE}{dt}(t) = \int_{-\infty}^{\infty} Q_{pad}(t - \tau) \frac{dE}{dt}(\tau) d\tau. \tag{4}$$

Finally, when considering an avalanche of electrons, the waveforms induced in each pad by each electron of the avalanche should be computed taking into account the arrival of each of them and summed in order to obtain the complete waveform (WF) of the avalanche.

Therefore, the numerical evaluation of the diffusion equation solution and of the convolution are extremely heavy in terms of computation time. To keep the simulation to a reasonable time some approximations were included as described below.

The first method is related to reducing the total number of avalanches to be simulated. The pad is divided into several smaller sub-pad regions e.g. 3×3 or 5×5. All the avalanches that are detected in the same pad sub-region

are merged into one and the charge  $Q$  is computed for the sum of all the contributions in this sub-pad.

The next and most significant optimization is related to the pre-computation of the diffusion equation solution and convolution. Before starting the simulation the detector response is pre-computed for a unit charge, a given RC that is input to the model, and for all the positions across a 2D grid in the pad,  $Q_{\text{unit}}(\text{RC}, x_i, y_i, t)$ , where  $x_i$  and  $y_i$  are the coordinates of a sub-pad center. The step of the grid can be tuned and for this work we divided the pad in a grid of  $10 \times 10$  sub-pad regions. The obtained distributions are convoluted with the derivative of the electronics response to get the waveform ( $WF_{\text{unit}}$ ) for a unit charge. The final waveform  $WF(t)$  can be easily obtained by scaling the pre-computed solution  $WF_{\text{unit}}$  with the total charge  $Q_i$  in each sub-pad  $i$  obtained from GEANT4, so that:

$$WF(t) = \sum_i Q_i \times WF_{\text{unit}}(x_i, y_i)(t). \quad (5)$$

The main approximation in this computation is the assumption that all the electrons in a sub-pad arrive at the center of this sub-pad. This implies that no numerical computations are needed during the simulation.

Two examples of the resulting WF, one for the data and one for the simulation, are shown in Fig. 4 for the leading and for two neighboring pads. Here and in the following of this paper, the leading pad is defined as the pad with the largest maximum of the waveform while neighboring pads are the ones adjacent to the leading pad in the direction perpendicular to the track (see discussion on clustering algorithms in Sect. 7).

The optimization methods described above reduce the computing time by more than two orders of magnitude without impacting the simulation output as it can be seen in Fig. 5 where no differences are observed in the charge ratio and time differences between the leading and the neighbour pad.

## 5. Characterization of ERAM detector

Each ERAM detector is scanned after production on an X-ray test bench at CERN. The test bench consists of a 3 cm width gas chamber and a robotic X-Y-Z arm system on an optical breadboard of  $120 \times 60$  cm<sup>2</sup> holding a 250 MBq <sup>55</sup>Fe source emitting 5.9 keV photons that deposit all their energy in the gas.

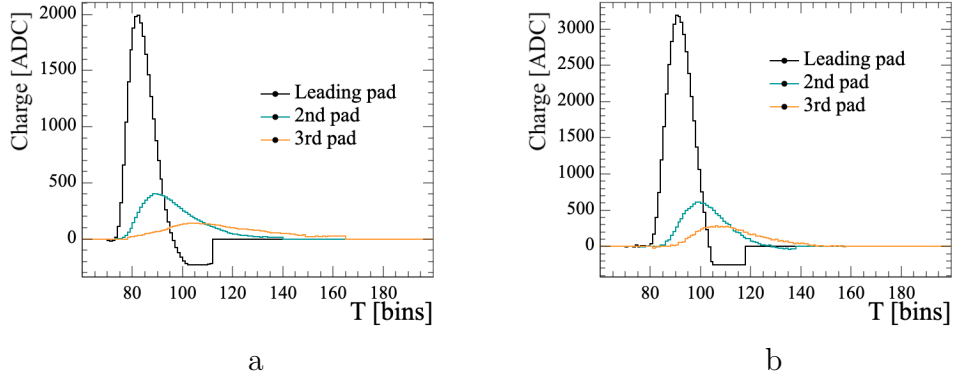


Figure 4: The example waveforms for the leading and adjacent pads in (a) data and (b) MC. The truncation of the underflow is due to the fact that in both, data and simulations, pedestals for each channel are equalized to 250 and, when the waveform goes below 0 they are set to 0. The 250 baseline is then subtracted offline and is not shown in the plot.

A 1.5 mm diameter collimation hole in front of the source assures that the majority of photo-electrons arrive on the targeted pad. Prior to the scan, the ERAM is aligned to ensure the position of the source with respect to the center of each pad.

Each channel of the ERAM is scanned for  $\sim 3$  minutes at a rate of 100 Hz, to reconstruct the spectrum of the  $^{55}\text{Fe}$  source and compute the gain for each pad. The gain is computed as the mean of the sum of the waveforms in a  $3 \times 3$  matrix around each channel. The map of the gain on the ERAM-01 and the gain uniformity are shown in Fig. 6.

The data from the test bench can also be used to measure the RC uniformity of the ERAM. This measurement campaign will be a subject of a future publication. For the comparisons between data and simulations that will be presented in this paper, we assumed uniform gain and RC in the simulation.

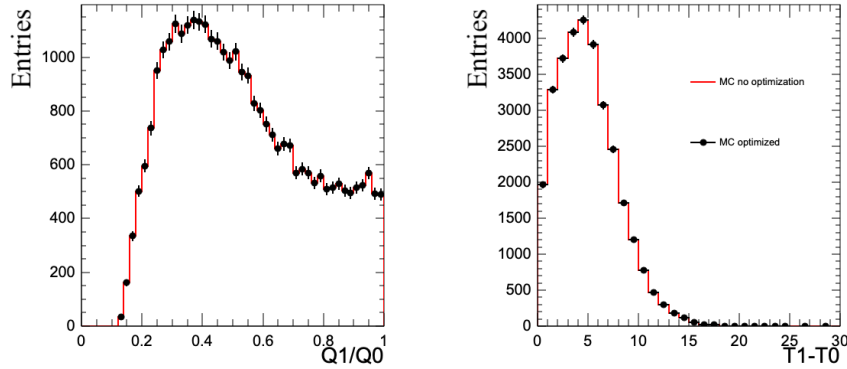


Figure 5: Charge ratio (left) and time difference (right) between leading and neighbour pad with and without the optimization needed to reduce computation time.

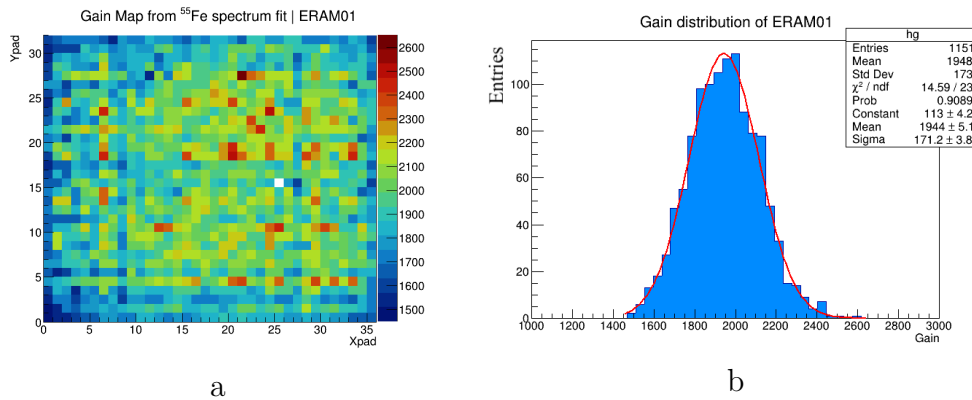


Figure 6: XY-map of the gain (a) and gain distribution (b) obtained with a  $^{55}\text{Fe}$  source for the ERAM used in the test beam. The channel (25,16) is a dead channel on ERAM-01.

## 6. Data collected at DESY

The tests at DESY were aimed to ensure that the HA-TPC prototype design fully satisfies the requirement of the ND280 upgrade for drift distances up to 97.25 cm that corresponds to the maximum drift length of the HA-TPC. Therefore, this test beam covered all the possible tracking conditions of the final HA-TPC.

The High-Angle TPC prototype equipped with ERAM-01 was flushed with T2K gas mixture and tested at DESY T24/1 facility. The chamber was

placed inside the PCMAG solenoid providing a magnetic field up to 1.25 T and exposed to the electron beam with tunable momenta between 1 and 4 GeV/c. The solenoid is equipped with a movable stage that allows moving the detector along the horizontal and vertical directions, and rotating by  $\pm 45$  degrees around a vertical axis. The TPC holder can be manually rotated inside the magnet.

Most of the data were taken with the cathode High Voltage set at 26.7 kV corresponding to an electric field in the TPC of 275 V/cm and at  $B = 0.2$  T as used in T2K. This field configuration corresponds to a drift velocity of 7.9 cm/ps. In order to study the dependence on different parameters and configurations, various scans were performed.

Thanks to the PCMAG movable stage we could rotate the TPC, performing scans of the ERAM-01 in X and Y (by rotating the prototype) directions as well as scans in Z (drift distance).

This is particularly interesting because it allows a study of the impact on the performances of possible non-uniformities in the gain or in RC.

The drift distance scan was done for two values of the electronics peaking time of 412 ns and 200 ns.

The data were also collected for different rotation angles around the horizontal axis ( $\phi$  angle), within varying magnetic fields and for three drift distances, one close to the ERAM, one in the middle of the chamber, and one close to the cathode.

## 7. Reconstruction and selection of tracks

Both, simulated and test beam tracks were reconstructed with the same analysis framework that uses DBSCAN [26] algorithm and the PRF method (discussed in Sect. 9)

The track is composed by "clusters" that are groups of pads in the direction perpendicular to the track. In order to be selected, a track needs to cross the whole detector. Due to a large number of pads per cluster (multiplicity) induced by the ERAM, two close parallel tracks may not be separated by a gap and thus mis-reconstructed as one single track.

To reject such topology and also to remove superimposed tracks, a cut on the mean multiplicity of a track is applied. This cut depends on the track clustering algorithm that is used to reconstruct the tracks. As it was introduced in [18], we use horizontal and vertical clustering for tracks with incident angles below 30 degrees and above 60 degrees respectively, while

for inclined tracks we use a diagonal clustering algorithm in which pads are combined into clusters according to their diagonal.

The mean multiplicity depends on the reconstruction algorithm and on the peaking time for the electronics. It is shown in Fig. 7 for horizontal and inclined tracks at various drift distance and peaking time. For inclined tracks, the multiplicity tends to increase with the drift distance due to the transverse diffusion of the electrons while crossing the gas volume. For horizontal tracks, instead, this effect is hidden by the larger effect induced by RC.

For the analyses presented in this paper, we select tracks with mean multiplicity comprised between 2.4 and 3.2 (1.5 and 2.2) for horizontal (inclined) tracks with 200 ns peaking time. For 412 ns peaking time only horizontal tracks were taken and, for this sample, we required a mean multiplicity comprised between 2.7 and 3.6.

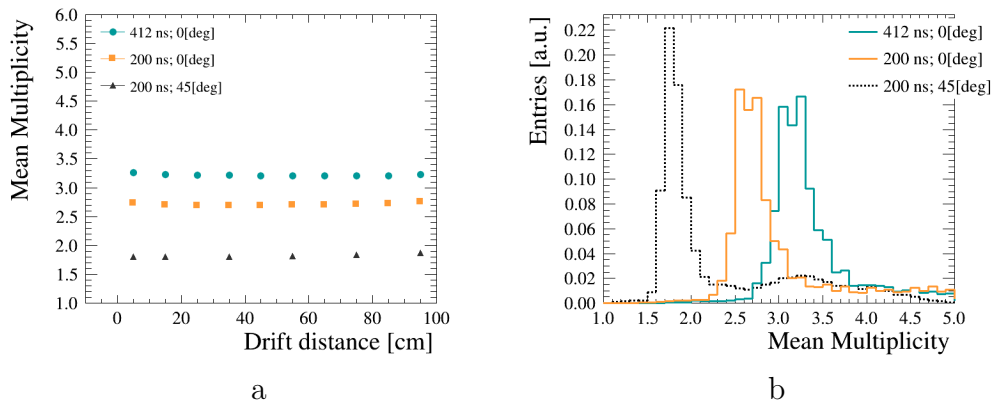


Figure 7: Mean multiplicity as a function of drift distance (a) and mean multiplicity profile (b) at different peaking time for horizontal and inclined tracks.

Finally, to avoid edge effects, the pads at the border are excluded from the reconstruction and hence horizontal tracks have 34 clusters while vertical tracks have 30.

## 8. ERAM response in data and simulation

To validate the simulation described in Sect. 4, we produced electrons propagating in the Y direction and compared some low-level variables describing the ERAM response, including charge sharing and time differences between neighboring pads in data and simulation. These comparisons are

done also with respect to the data taken at DESY in 2019 with a different ERAM module that is described in [18]. The comparison between data and simulation for spatial resolution and  $dE/dx$  resolution will be shown in Sect. 11.

The most important variables for the resistive feature characterization are the charge ratio and the time difference between the WFs observed in the adjacent pads and the one in the leading pad.

For these comparisons, the charge in the pad is defined as the maximum of the waveform and the time is defined as the time bin at which the waveform reaches its maximum. The pads in a cluster are then ordered according to their charge ( $Q_1$  and  $T_1$  refer to the pad with the largest charge,  $Q_2$  and  $T_2$  the second,  $Q_3$  and  $T_3$  the third).

Since these variables depend on the relative position of a track with respect to the pad center, we sampled the distributions based on the reconstructed track position. These distributions are shown in Fig. 8 for 5 cm drift distances.

In order to make a more quantitative comparison between data and Monte Carlo, the distributions of Fig. 8 were fit with the Landau function and the most probable value (MPV) is plotted in Fig. 9 for these data (DESY 2021), the one from the previous test beam (DESY 2019) and MC samples generated with  $RC=55$  ns/mm<sup>2</sup> and  $RC=100$  ns/mm<sup>2</sup>.

This comparison clearly shows the different behavior of the two ERAM modules, especially for what concerns the time differences that are most affected by RC.

The difference in the data can be explained by a different value of RC between the two modules. The data from 2021 are better reproduced by using  $RC=100$  ns/mm<sup>2</sup>, however, even for this RC value, some visible differences between the data and simulation are observed. As we will show in Sect. 11, these differences do not affect the detector performances in terms of spatial or energy resolution.

The charge ratio and time differences for larger drift distances, where effects induced by the diffusion in the gas play an important role, show in general a better agreement between data and simulation, as illustrated in Fig. 10.

For the future, we expect to improve the agreement between data and MC by using in the simulation the value of RC that will be measured with the Test Bench described in Sect. 5 and taking into account possible non-uniformities within the detector.

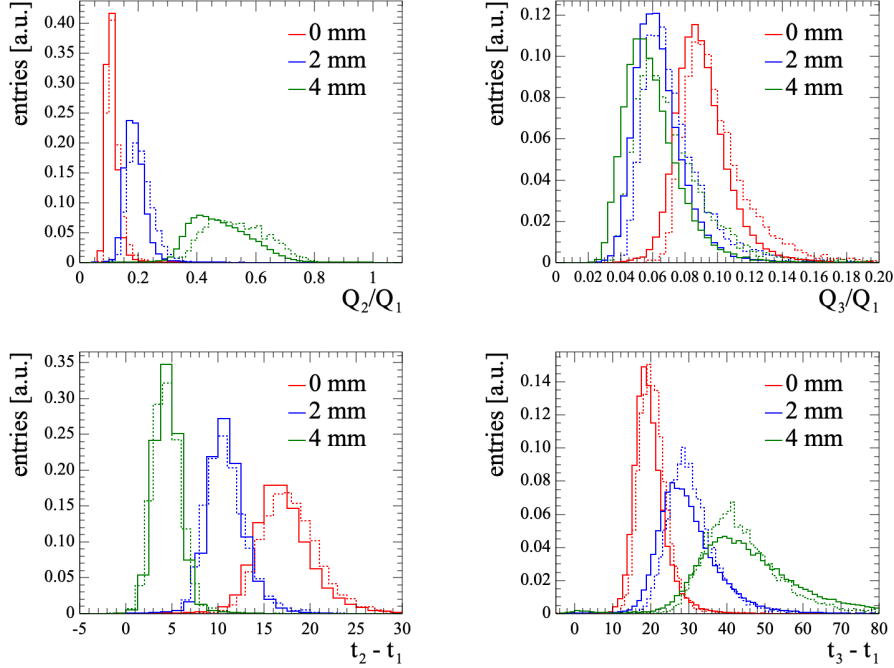


Figure 8: Ratio of the charge in the second pad (top left) and third pad (top right) with respect to the leading pad and time difference between leading and second (bottom left) and third pad (bottom right) as a function of the reconstructed distance from the pad center. The solid lines represent data (DESY 2021) and the dashed ones are the simulation.

## 9. Spatial resolution

The ND280 TPCs measure the momenta of the outgoing particles from neutrino interactions in order to reconstruct the energy of the incoming neutrino, one of the critical elements for precise measurement of neutrino oscillations parameters.

The TPC momentum resolution depends on the spatial resolution (SR) [27] that can be characterized with test beam data. For this analysis, the spatial resolution is measured by employing a “pad response function” (PRF) in the same manner as in [19, 18].

In this method we define, for each cluster, the residual as the difference between the position of the track reconstructed locally (e.g. in one column) and the fitted track position. The distribution of the residuals in each cluster is fitted with a Gaussian and its width represents the spatial resolution.

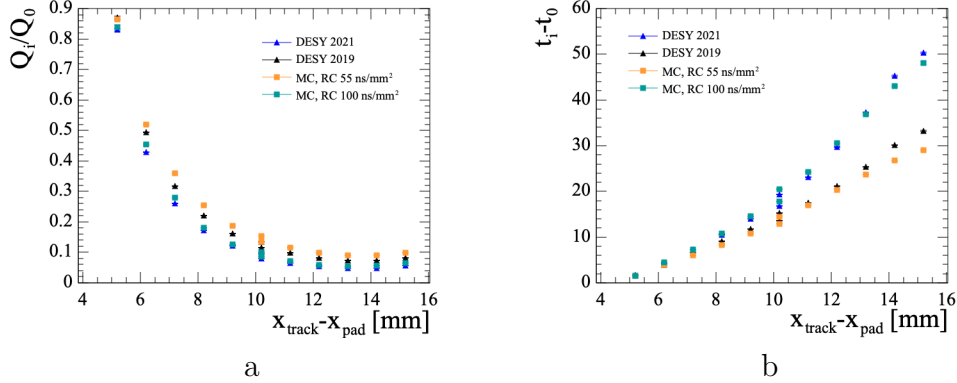


Figure 9: The comparison of the MC simulations and two test beams (DESY 2021 and DESY 2019) for the charge ratio (a) and time difference (b) between leading and adjacent pads as a function of the difference between pad center ( $x_{pad}$ ) and reconstructed track position ( $x_{track}$ ). Two points are shown for  $x_{track} - x_{pad} = 10$  mm because, for tracks in the center of the pad, the two adjacent pads have the same distance from the track.

The measurement of the track position is performed with an iterative procedure. For the first step, all the tracks are reconstructed using the charge barycentric method. Such a method estimates the position of the track in a certain cluster by weighting the centre of the pad position by the charge in this pad. The estimated primary track positions in each cluster are then fit with a parabola over the whole detector (global fit). Based on the results of the fit, a pad response function scatter plot is filled for each pad. The PRF function is defined as:

$$PRF(x_{track} - x_{pad}) = Q_{pad}/Q_{cluster} \quad (6)$$

where  $x_{track}$  and  $x_{pad}$  are positions of the track from the global fit and the center of the pad, respectively, and  $Q_{pad}$  and  $Q_{cluster}$  are charges collected by the pad and by the whole cluster.

The PRF scatter plot is fitted with a ratio of two polynomes (the same as in [18, 28]). The scatter plot and the parametrization of the PRF are done independently for samples at different drift distances and inclination. The estimated parameters of the PRF analytical function are used further in the  $\chi^2$  minimization procedure to estimate the track position in each cluster.

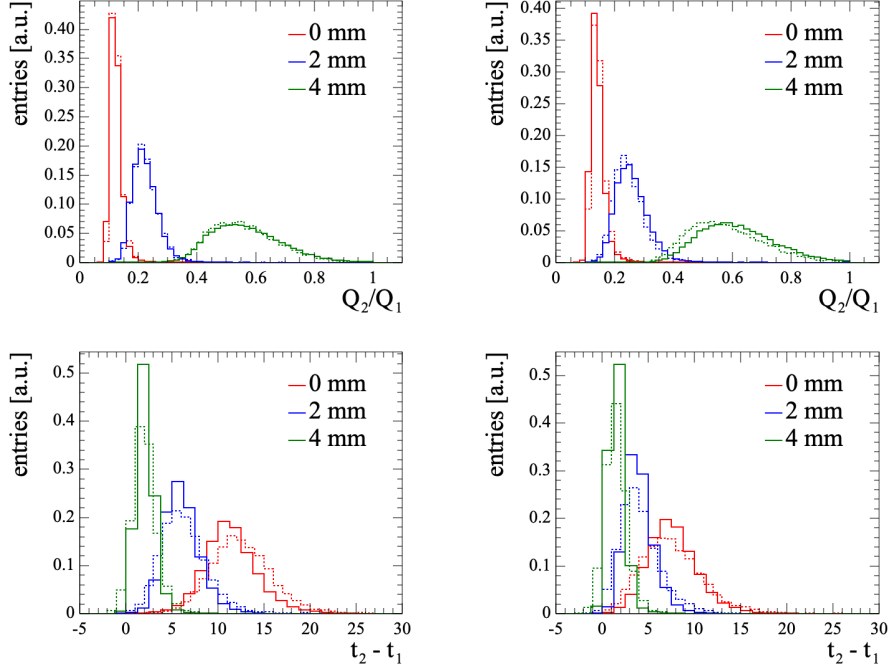


Figure 10: Charge ratio between second and leading pad for drift distances of 50 cm (top left) and 90 cm (top right) and time difference between first and second pad for drift distances of 50 cm (bottom left) and 90 cm (bottom right) as a function of the reconstructed distance from the pad center. The solid lines represent data (DESY 2021) and the dashed ones are the simulation.

$$\chi^2 = \sum_{pads} \left( \frac{Q_{pad}/Q_{cluster} - PRF(x_{track} - x_{pad})}{\sigma_{Q_{pad}/Q_{cluster}}} \right)^2 \quad (7)$$

where  $\sigma_{Q_{pad}/Q_{cluster}} = \sqrt{Q_{pad}/Q_{cluster}}$ .

In the following iterations the track position was evaluated from the fit. The iteration procedure is repeated while the spatial resolution keeps improving and it typically converges after three iterations. Examples of PRF for horizontal and inclined tracks are shown in Fig. 11. A small dip around zero can be observed in PRF for inclined tracks. This is due to the width of the distribution around zero and to the freedom of the polynomial fit.

The spatial resolution was defined as a mean of the residual distribution for each cluster. Examples for horizontal and inclined tracks are shown in

Fig. 12. The distribution is expected to be centered at zero and differences with respect to zero are the biases that will be discussed in Sect. 9.3.

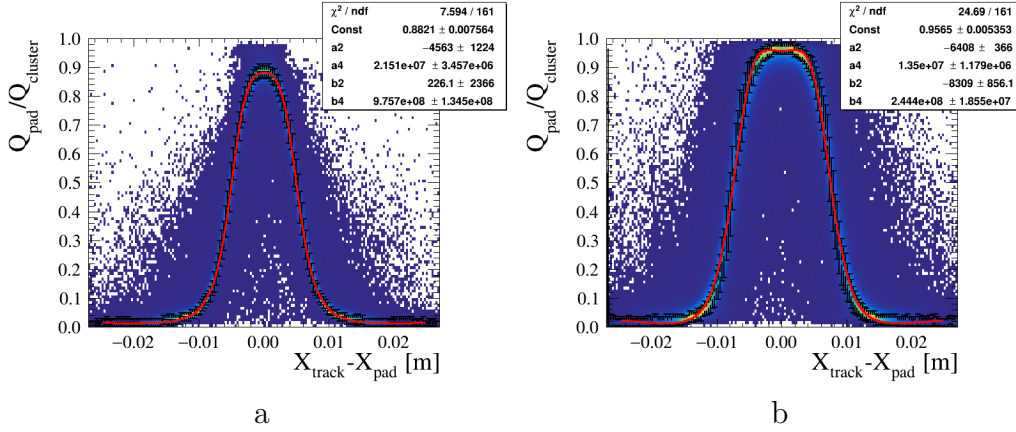


Figure 11: PRF function for (a) horizontal and (b) inclined tracks.

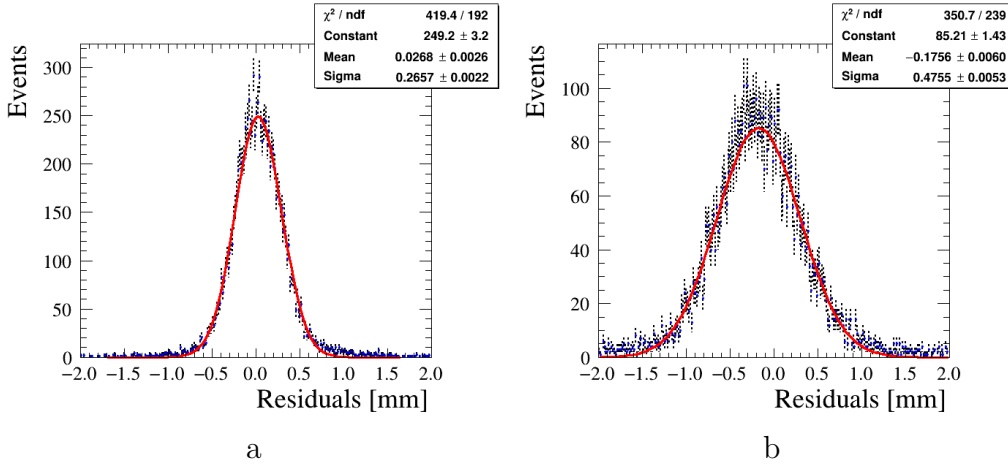


Figure 12: Residuals distribution for single cluster for (a) horizontal and (b) inclined tracks.

As an external cross-check of the performance of tracking algorithm, typical distributions of reconstructed track position for incoming electron beam are shown in Fig. 13.

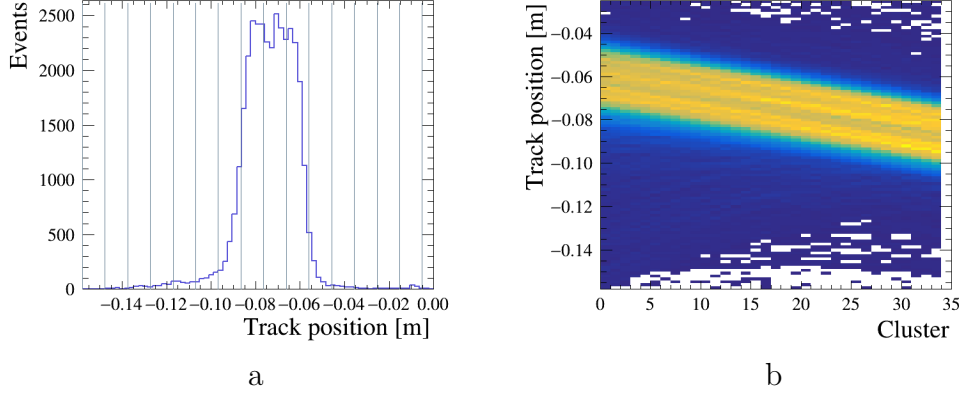


Figure 13: A typical distribution of the reconstructed track position for incoming electron beam (a), where the vertical lines correspond to the center of each pad and reconstructed track position with respect to the cluster number (b).

### 9.1. Spatial resolution for horizontal tracks

With this method we can evaluate the spatial resolution for different track topologies. The results for the horizontal tracks as a function of the drift distance for different electronics peaking time are presented in Fig. 14.

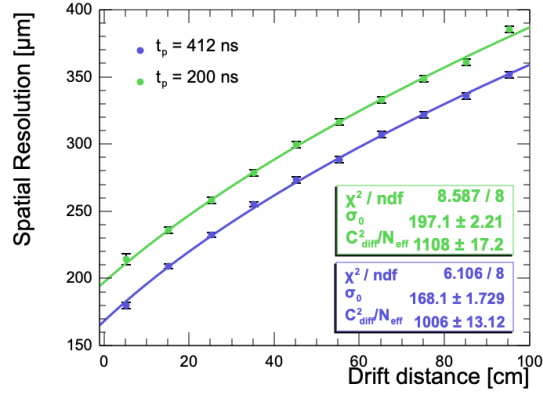


Figure 14: Spatial resolution with respect to the drift distance for the beam parallel to the pad side with a magnetic field of 0.2 T, and peaking times of 200 ns and 412 ns.

The resolution over the drift distance is expected to follow this dependence.

$$\sigma(Z) = \sqrt{\sigma_0^2 + C_{diff}^2/N_{eff} \times Z} \quad (8)$$

where  $\sigma_0$  is the resolution at null drift distance,  $C_{diff}$  is the transversal diffusion constant and  $N_{eff}$  is the number of effective electrons [29]. The observed dependence is in agreement with this prediction. The peaking time mildly affects the  $C_{diff}^2/N_{eff}$  term, but changes the  $\sigma_0$ . A larger peaking time results in a higher amplitude in the neighbour pads and higher pad multiplicity. Thus we have more robust information for the PRF fit and the track position reconstruction is more precise.

The spatial resolution can also depend on the ERAM module characteristics, such as its gain and the local RC value. To investigate these possible dependencies we used a scan done at fixed drift distance but with horizontal tracks crossing the ERAM at different X positions and vertical tracks crossing the ERAM at different Y positions. The spatial resolution obtained for these different X and Y positions is shown in Fig. 15. No large differences are observed indicating that possible local non-uniformities on the ERAM module do not affect the spatial resolution.

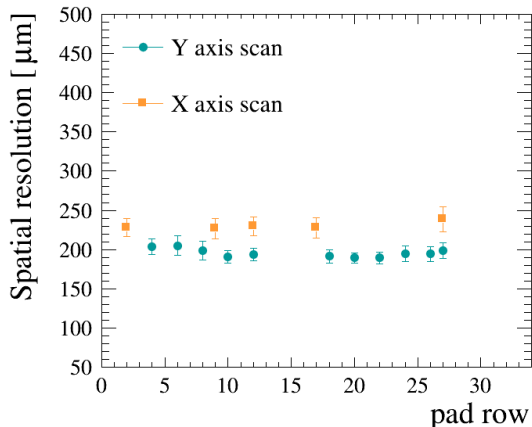


Figure 15: Spatial resolution for different Y and X positions at 412 ns peaking time.

### 9.2. Spatial resolution for inclined tracks

The collected test beam data allow studying spatial resolution as a function of the angle of inclination of the tracks within the ERAM module plane. The novelty with respect to the studies performed in [18] is that we could

evaluate the spatial resolution performances for inclined tracks at long drift distances. The results are presented in Fig. 16 (a), where angles from 0 to 30 degrees and from 70 to 90 clusters are defined perpendicular to the track direction (horizontal/vertical fit), and for the highly inclined tracks, with the angle between 40 and 60 degrees, the clusters defined along the diagonals as described in Section 7. In [18] it has been shown that the use of a diagonal fit for highly inclined tracks significantly improves the spatial resolution with respect to the use of horizontal or vertical fits.

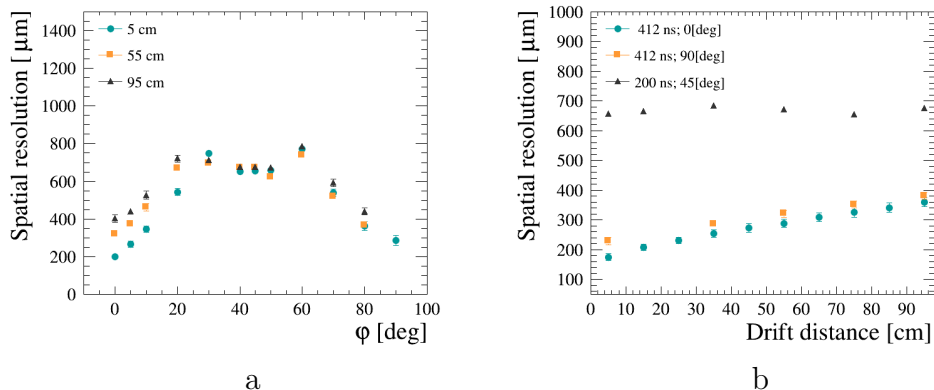


Figure 16: Spatial resolution for different angles of the electron tracks inclination in the pad plane with 200 ns peaking time, 0.2 T magnetic field and for various drift distances: 5 cm, 55 cm, 95 cm (a) and spatial resolution versus drift distance for horizontal (0 deg.), inclined (45 deg.) and vertical (90 deg.) tracks.

Fig. 16 (a) demonstrates that, while the spatial resolution depends on the angle, it stays between 200 and 800  $\mu\text{m}$  for all the analyzed samples. In particular, it is interesting to notice in Fig. 16 (b) that, while the spatial resolution degrades with the drift distance for horizontal and vertical tracks, it is constant for inclined tracks.

The behavior for diagonal tracks can be understood considering that the spatial resolution depends on the charge spread over a certain amount of pads (multiplicity). A diagonal clustering algorithm leads to a smaller mean multiplicity than in the case of horizontal/vertical fit as it was shown in Fig. 7. With the diagonal fit pad size becomes effectively  $\sqrt{2}$  times larger, thus degrading the spatial resolution but also making the effect of the transverse diffusion less significant.

Moreover, diagonal fit implies a dependence of the resolution on the length

of the track in the cluster. This causes an oscillatory behavior in the spatial resolution versus the cluster that is shown in Fig. 17 (a). Fig. 17 (b) shows the dependence of the spatial resolution on the track length per cluster for inclined tracks. It is clearly seen that, as expected, the resolution improves for longer track segment lengths within the cluster.

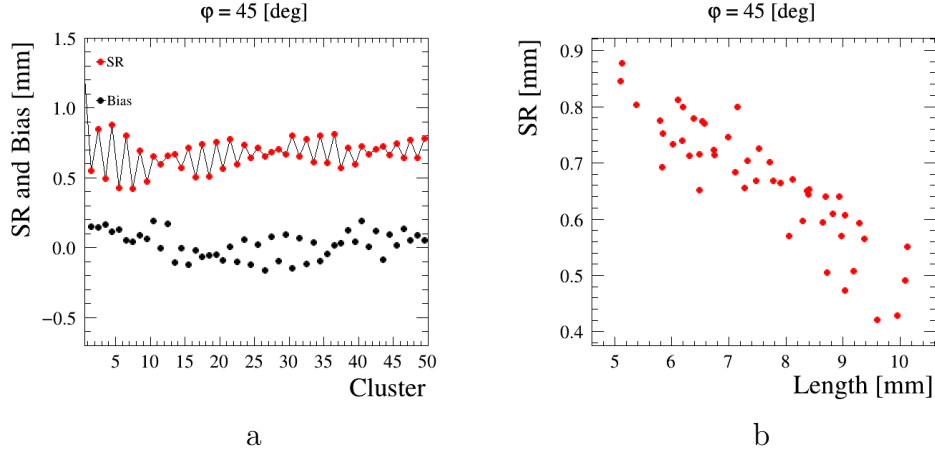


Figure 17: Tracks of 45 degrees inclination: spatial resolution per cluster (a) and spatial resolution with respect to mean track segment length in a cluster (b).

### 9.3. Biases in spatial resolution

The bias of the track position in each cluster of the ERAM pad plane is defined as the mean of the Gaussian fit of the distribution of residuals per cluster, and can be referred to as the systematic uncertainty of the track position estimation. In [18, 30] it is shown that the biases depend on the track position. The data collected during this campaign allow a deeper study of biases, in particular their dependence on drift distance for both horizontal and inclined tracks, as well as their behavior for various magnetic field strengths (see Sec. 12).

Fig. 18 (a) shows the bias as a function of the drift distance for horizontal tracks. In this figure, the bias is defined as the mean of the absolute values of the biases per cluster. It is observed that biases are larger at short and long drift distances than at distances corresponding to the middle of the drift volume.

For inclined tracks, instead, as shown in Fig. 18 (b), the biases do not depend on the drift distance or on the  $\phi$  angle of the tracks reconstructed using diagonal clustering.

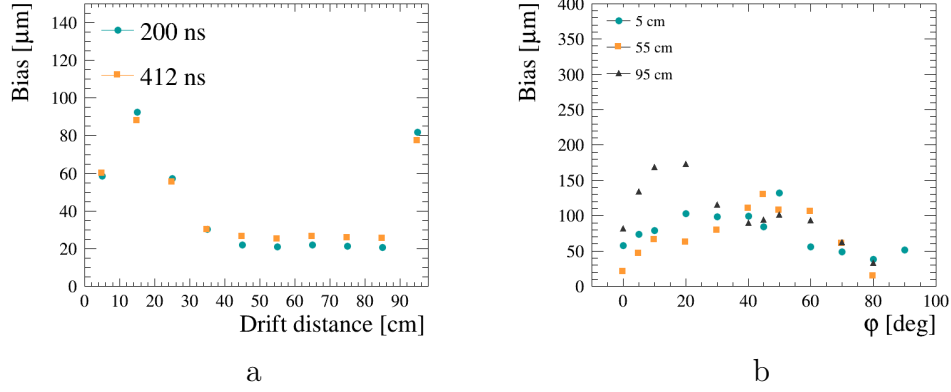


Figure 18: Track position bias with respect to the drift distance for the beam parallel (a) and inclined (b) to the pad side with a magnetic field of 0.2 T, and peaking time of 200 ns.

In order to further investigate the behavior observed in Fig. 18, the dependence of the spatial resolution and bias per column on the drift distance is shown in Fig. 19. For the smallest and largest drift distances, biases have visible patterns with large and opposite biases at the beginning and at the end of the track. This pattern is not observed for tracks in the center of the ERAM.

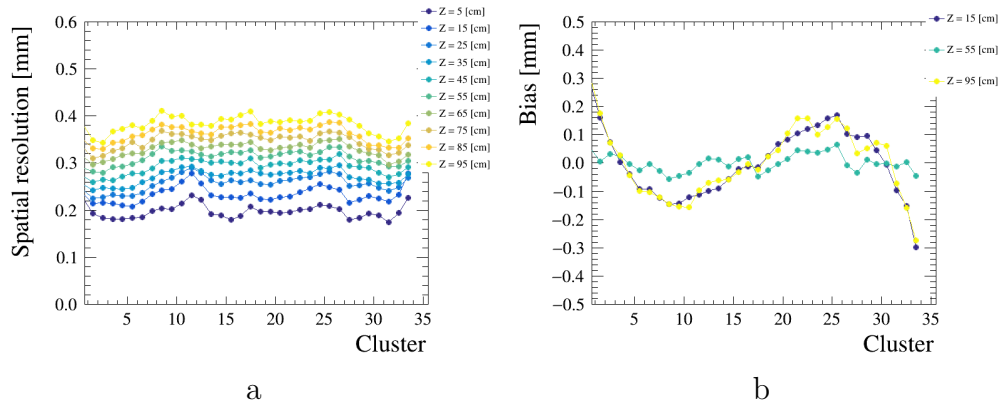


Figure 19: Spatial resolution (a) and track position bias (b) distributions per cluster for the beam parallel to the pad side with a magnetic field of 0.2 T, and peaking times of 200 ns at various drift positions (z axis).

The observed dependencies of the biases are not reproduced by the sim-

ulation and can point to effects related to non-uniformities in the magnetic field, not accounted for in the simulation, and the  $E \times B$  effect. In Sect. 12 we will discuss the impact of these effects on the observed tracks, together with a study of the observed biases as a function of the applied magnetic field.

For all the configurations the biases are below 200  $\mu\text{m}$  and their size is small with respect to the spatial resolution for highly inclined tracks.

## 10. $dE/dx$ resolution

The other main goal of the HA-TPC is to perform particle identification by measuring the deposited energy by charged particles crossing the gas. The TPC particle identification capability will depend on the  $dE/dx$  resolution that can be evaluated with the data from this test beam.

In the context of T2K it is particularly important to be able to distinguish electrons and muons. Such an effort is crucial to estimate electron neutrinos contamination in the muon neutrino beam and to predict the expected number of un-oscillated electron neutrinos in the far detector. To distinguish electrons and muons the deposited energy resolution requires to be better than 10% in order to achieve a more than  $3\sigma$  separation between electrons and muons.

The deposited energy is calculated per track using the truncated mean method already introduced in [18].

The method consists in calculating the track mean deposited energy by summing the deposited energy in the reduced number of clusters fired by the electron and ignoring the fraction of those that have a large energy contribution. Such contribution is caused by fluctuations in the ionization processes and leads to the smearing of the energy spectrum.

The truncation factor is optimized with the data and we found it to be 0.7 which is the same as for the DESY 2019 test beam data [18]. This means that 70% of the clusters are kept for deposited energy calculations.

The deposited energy per cluster was calculated by taking the maximum of the sum of the waveforms of the pads constituting the cluster. Various cluster charge definitions were studied in [18] and it was shown that the charge defined using the sum of the waveforms results in a better deposited energy resolution.

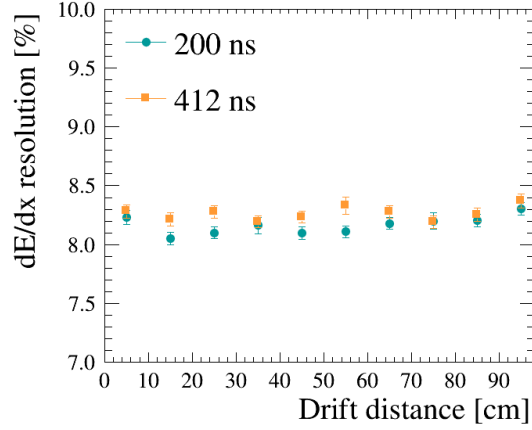


Figure 20:  $dE/dx$  resolution with respect to the drift distance for the beam parallel to the pad side with a magnetic field of 0.2 T, and peaking times of 200 ns and 412 ns.

The deposited energy resolution was measured for both parallel and inclined tracks with respect to the pad side. Fig. 20 shows the deposited energy resolution measured for the parallel tracks for various drift distances.

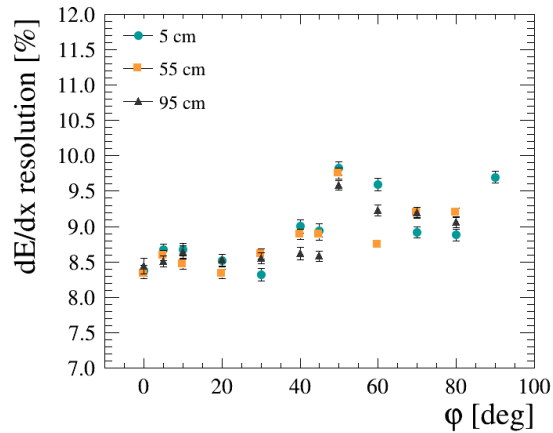


Figure 21:  $dE/dx$  resolution versus different angles of the electron tracks inclination in the pad plane with 200 ns peaking time, 0.2 T magnetic field and for various drift distances: 5 cm, 55 cm, 95 cm. A 10% discrepancy observed around  $\phi = 60^\circ$  is under study.

Fig. 21 shows the  $dE/dx$  resolution at various drift distances as a function of the angle within the pad plane.

Additionally, the deposited energy for tracks reconstructed with the diagonal fit was corrected for the track length in each cluster. Such correction accounts for the non-linear dependence of the charge with respect to the track length caused by the charge contribution from the neighbouring clusters for short track cluster length.

The study shows that the  $dE/dx$  resolution is  $\sim 8.5\%$  for horizontal tracks and stays between  $7.5\%$  and  $9.6\%$  for inclined and vertical tracks. Furthermore, it is independent of drift distance and of the electronics peaking time. It has been observed that  $dE/dx$  resolution is controlled by balancing two factors: the mean charge per cluster and the number of clusters. Fig. 21 shows that  $dE/dx$  resolution worsens for the angles  $> 45$  degrees since for such angles a smaller number of clusters is reconstructed per track due to the rectangular shape of the ERAM.

Finally, as in the case of spatial resolution, we looked for effects due to non-uniformities of the ERAM by using the X and Y scans. The results are shown in Fig. 22. We observe some differences, possibly due to non-uniformities in the gain of the ERAM, but in general, the resolution is below  $10\%$  for all the Y and X scans.

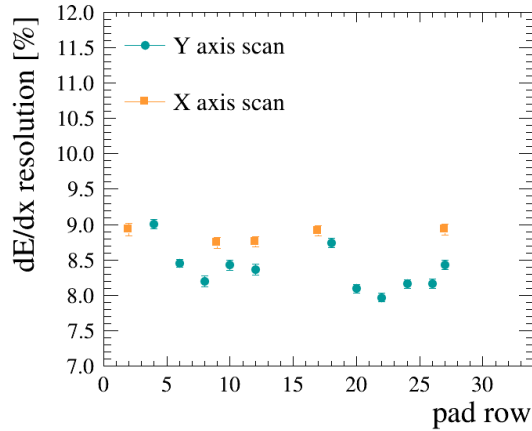


Figure 22:  $dE/dx$  resolution for tracks entering the ERAM at different X and Y positions.

The observed results prove that the ERAM energy resolution fulfills the requirements for the ND280 upgrade.

## 11. Comparison between data and simulation

In this section we compare the performances of the ERAM for spatial and dE/dx resolution between data and simulation.

Fig. 23 shows the spatial resolution for the data and MC samples as a function of the drift distance. The dependence over the drift distance was found to be slightly different using the default value used in the ND280 simulations of the vertical TPC that has a transverse diffusion  $\sigma_{trans} = 286 \mu\text{m}/\sqrt{\text{cm}}$ . The diffusion can be affected by the magnetic field configuration as well as environmental conditions such as temperature and pressure, or by the amount of oxygen and water contamination in the chamber.

We made simulations with different values of  $\sigma_{trans}$ . As expected, in general, increasing  $\sigma_{trans}$  results in a worst spatial resolution for large drift distances. A satisfactory agreement was found by increasing the transverse diffusion by 8%, changing it to  $\sigma_{trans} = 310 \mu\text{m}/\sqrt{\text{cm}}$ . Furthermore, while in the data we observe a dependence on the drift distance in good agreement with the one expected from Eq. 8, in the simulation we find that this dependence is linear. The origin of this difference between data and simulation is under investigation.

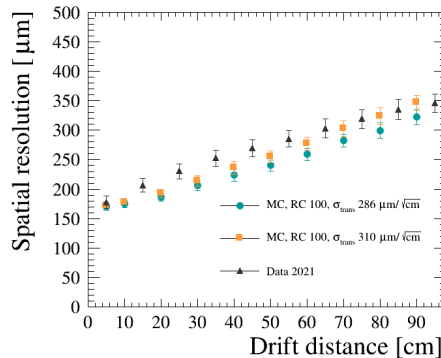


Figure 23: Spatial resolution over the drift distance for DESY 2021 data at 412 ns peaking time and MC samples generated with different values of transverse diffusion at 400 ns peaking time.

In Fig. 24 (a) we show the comparison in the spatial resolution between data and simulation for tracks at different angles. It should be noticed that the  $\phi$  scan was done using different electronics peaking times and we did the

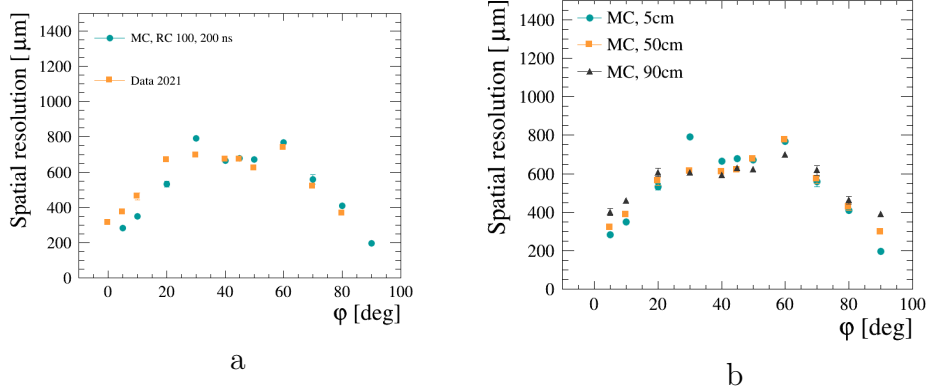


Figure 24: Spatial resolution over angle with respect to pad borders for (a) data and MC samples at 200 ns peaking time and 55 cm drift distance and (b) simulation for the different drift distances.

simulation for the two cases. The simulation rather correctly reproduces the behaviour observed in the data.

In Fig. 16 (b) it was found that the spatial resolution weakly depends on the drift distance for the highly inclined tracks. This effect was cross-checked and confirmed with the simulation. Fig. 24 (b) shows large effect of the drift distance on the tracks close to  $0^\circ$  and  $90^\circ$ , but much smaller effect at  $45^\circ$ .

Concerning the deposited energy resolution, the simulation reproduces reasonably well the data for both, horizontal and inclined tracks, as shown in Fig. 25.

## 12. $\mathbf{E} \times \mathbf{B}$ effect

Inhomogeneities in the magnetic field can create distortions of the image of the track projected on the ERAM. These distortions are not expected to impact the spatial resolution that is computed based on the track image on the ERAM, but can affect the determination of the reconstructed momentum. This effect is expected to be small in ND280, where the magnetic field inside the magnet has been measured with a dedicated campaign [1], and can be larger in the PCMAG used in DESY, where inclined tracks were observed even for a horizontal beam, as shown in Fig. 26.

It is worth saying that this effect cannot be explained by the curvature induced by the magnetic field that is negligible for the operational magnetic field and electron momenta used in the test beam.

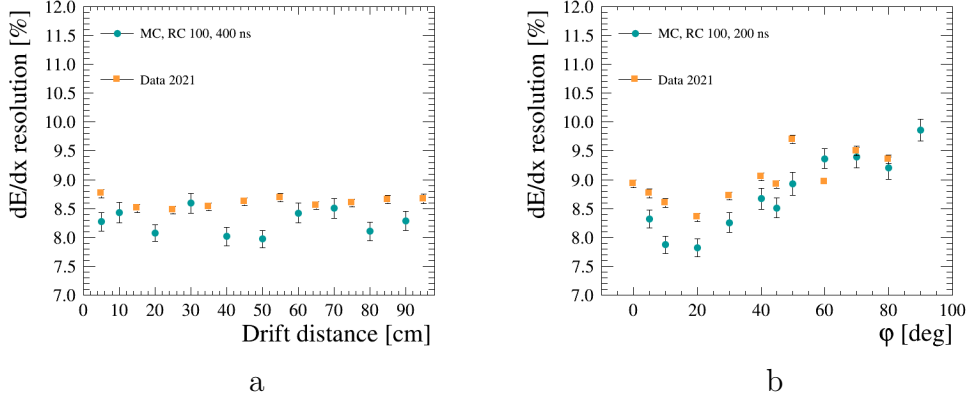


Figure 25: dE/dx resolution in data 2021 and MC for (a) horizontal tracks (at 412 ns peaking time) as a function of the drift distance and for (b) inclined tracks (at 200 ns peaking time) as a function of the track inclination angle. The dE/dx is calculated using the sum of the cluster charge.

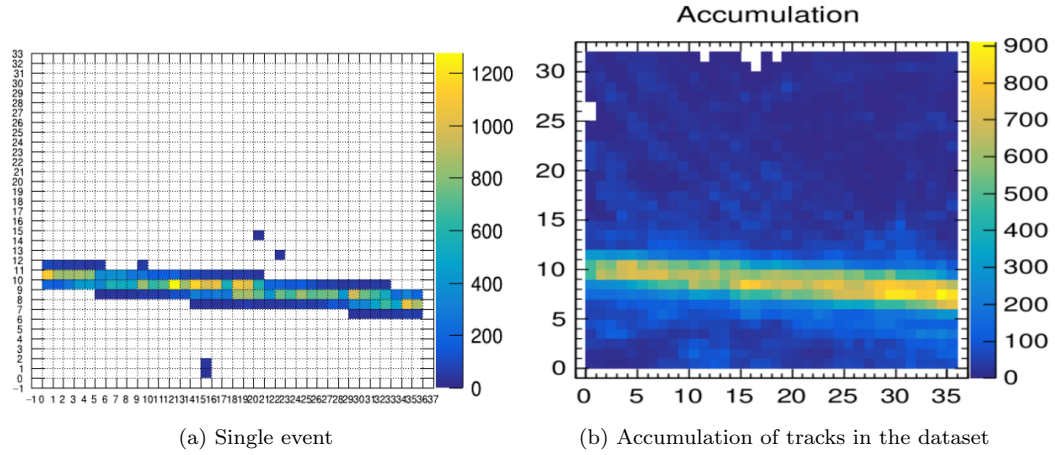


Figure 26: Event display of nominally horizontal beam. (a) single track; (b) accumulation plot of the tracks from the same dataset ( $B = 0.2$  T).

Compelling arguments support the hypothesis of “ $E \times B$  effect” accounting for the inclination of tracks projected on the ERAM. Below we present the explanation of the effect. The drift velocity is given by the Langevin equation:

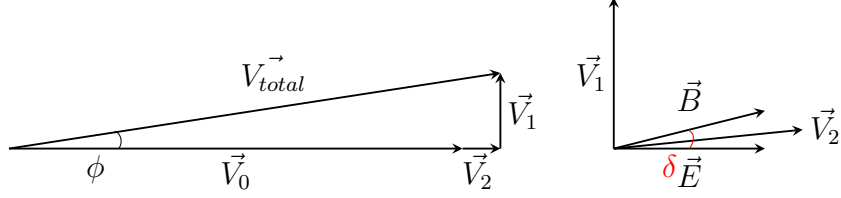


Figure 27: Schematic view of the drift velocity components according to the Langevin equation.

$$\vec{V}_d = \frac{\mu}{1 + (\omega\tau)^2} \left( \vec{E} + (\omega\tau) \frac{\vec{E} \times \vec{B}}{|\vec{B}|} + (\omega\tau)^2 \frac{\vec{B} \cdot (\vec{E}\vec{B})}{|\vec{B}|^2} \right), \quad (9)$$

where  $\mu = \frac{e}{m}\tau$  is the electron mobility in the gas,  $\omega = \frac{eB}{m}$ , and  $\tau$  is the time between two collisions.

The scheme visualizing the drift velocity components is shown in Fig. 27, in which we have defined the components of  $\vec{V}_d$  as  $\vec{V}_0 = \frac{\mu}{1+(\omega\tau)^2}\vec{E}$ ,  $\vec{V}_1 = \frac{\mu}{1+(\omega\tau)^2} \cdot (\omega\tau) \frac{\vec{E} \times \vec{B}}{|\vec{B}|}$  and  $\vec{V}_2 = \frac{\mu}{1+(\omega\tau)^2} \cdot (\omega\tau)^2 \frac{\vec{B} \cdot (\vec{E}\vec{B})}{|\vec{B}|}$ . The angle between the electric and magnetic field is defined as  $\delta$  so that  $|\vec{E} \times \vec{B}| = EB \sin(\delta)$ .

Assuming small  $\delta$ , the  $\vec{V}_2$  component aligns with  $\vec{V}_0$  component. Then the drifting electrons will move transversely in the  $\vec{V}_1$  direction and will be projected on the ERAM with a shift  $\Delta$ :

$$\Delta = Z_{drift} \times \left\langle \frac{v_y}{v_z} \right\rangle = Z_{drift} \times \left( \frac{\langle \delta \rangle \omega\tau}{1 + (\omega\tau)^2} \right) \quad (10)$$

where  $Z_{drift}$  is the drift distance and  $\langle \delta \rangle$  is the average value of  $\delta$  along the trajectory of the drifting electron.

Since  $\langle \delta \rangle$  varies along the track, an apparent inclination of the track is observed which can be evaluated with  $\phi_{app}$ :

$$\phi_{app} = \text{atan} \left( \frac{y_L - y_R}{X_{ERAM}} \right) \quad (11)$$

where  $X_{ERAM}$  is the width of the ERAM (40.6 cm) and  $y_L$  and  $y_R$  are the track vertical positions on the Left and Right edges.

It follows from Eq. (10) that the apparent inclination due to  $E \times B$  effect is maximum for  $\omega\tau = \mu B = 1$ . In our case, where the electron mobility is

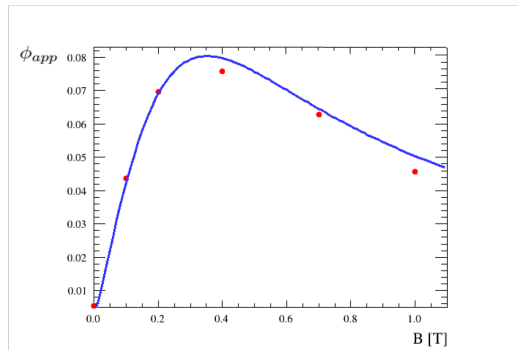


Figure 28: The red points show the dependence of observed track inclination on the magnetic field strength. Assuming that the  $\delta$  values at each end of the track are opposite, these inclinations correspond to twice the displacement given by Eq. 11. The theoretical prediction is shown in blue; the model depends only on  $|\delta|$  and the fit finds  $|\delta| = 0.018$  as the best estimate. Notice the slight deviation for high magnetic field, where the bending effect of the longitudinal magnetic field starts to be relevant.

expected around  $\mu = 2.8 \text{ T}^{-1}$ , this means  $B \simeq 0.36 \text{ T}$ , which is consistent with what Fig. 28 shows.

As it can be seen in Fig. 26, the electrons drifting to the leftmost region of the ERAM are shifted upwards, while the ones drifting to the rightmost region are shifted downwards. The displacements perpendicularly to the track depend on the component of the magnetic field on the track direction. It turns out that this component flips sign when the track crosses the inner volume of the PCMAG solenoid due to the symmetry of the radial components of its field.

To study this effect, we simulated the motion of drifting electrons with Garfield++ [31], under the proper electric and magnetic field conditions and the gas mixture used in the detector. For the magnetic field, we use the map based on previous measurements at DESY [32] and shown in Fig. 29. For the electron mobility the value  $\mu = 2.84 \text{ T}^{-1}$  was used in the simulation.

From both data and simulation, we compute the inclination of tracks projected on the ERAM, and compare the results. Fig. 30 shows that the simulation is able to reproduce the vertical displacement of drifting electrons as observed in the data.

The  $E \times B$  effect dependence on the magnetic field is shown in Fig. 31 for different values of magnetic field and different drift distances. As expected, without the magnetic field, there is no displacement in Y. When the magnetic

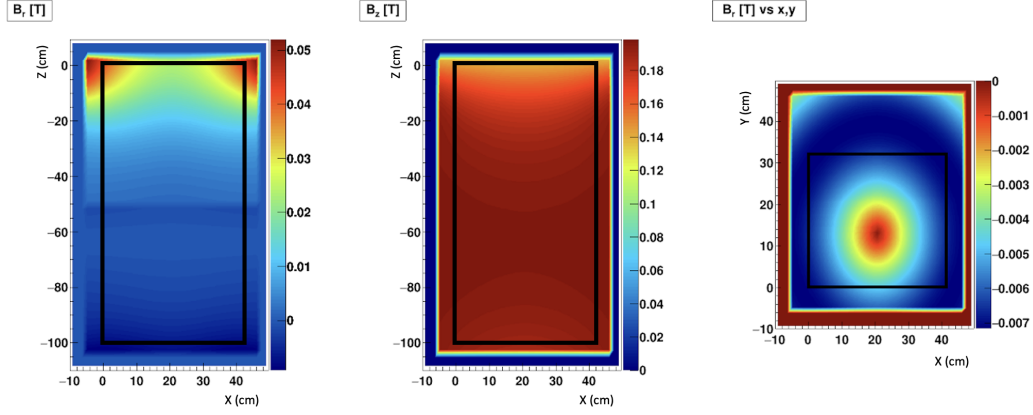


Figure 29: Map of the magnetic field. Left: radial component, top view. Central: longitudinal component, top view. Right: radial component, front view. The black boxes represent the contours of the TPC's drift volume. Notice the non-negligible radial component of the field, especially in the rear of the TPC.

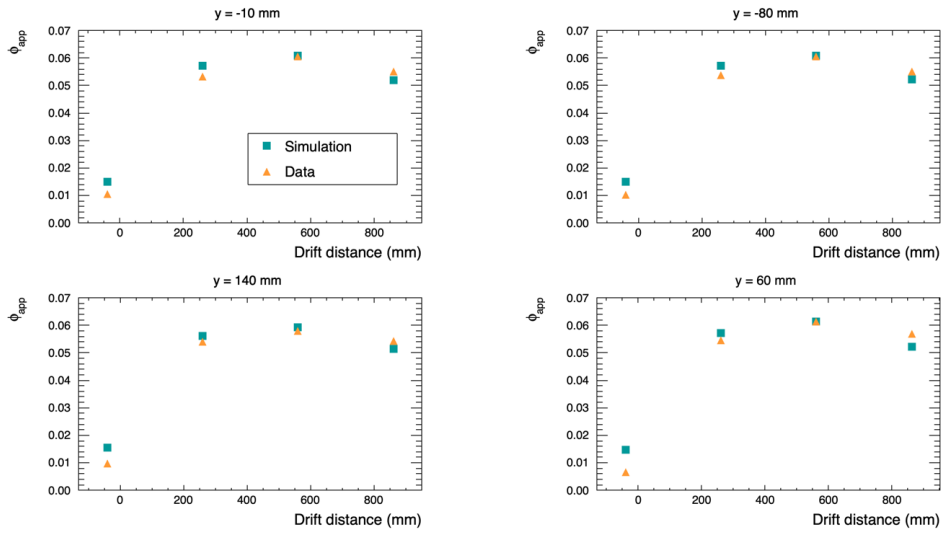


Figure 30: Track inclinations in data and simulations for  $B = 0.2$  T. Each plot represents a different vertical position of the initial ionization track. The simulation uses Garfield++ [31] as described in the text.

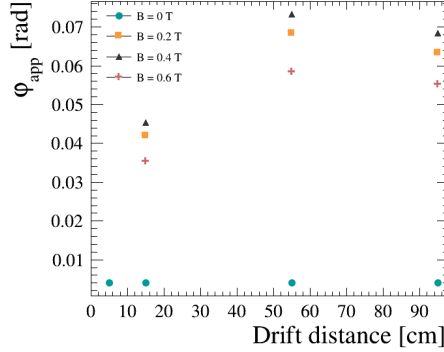


Figure 31: Track inclinations with respect to the drift distance for the beam parallel to the pad side for different values of magnetic field at the drift velocity of  $78.7 \text{ cm}/\mu\text{s}$  and peaking time of 200 ns.

field is on, as expected, a larger displacement is observed for small values of the magnetic field.

The  $E \times B$  effect generates displacements of the charge landing position on the anode surface which result in the observed inclination of the tracks. However, these displacements do not scale linearly along the track and deviations from the inclined direction are expected which could explain the biases observed in the spatial resolution described in Sect. 9. Further investigations are ongoing on this point but it is already clear that these biases share the same behavior with respect to the magnetic field as the  $E \times B$  effect reported above.

In Fig. 32 we show the biases in the spatial resolution for different values of the magnetic field and as a function of the drift distance. The biases are small for all the drift distances when the magnetic field is off. When the magnetic field is on we observe larger biases for short and long drift distances, similar to the ones shown in Fig. 19. The larger biases are observed for values of the magnetic field of 0.2 and 0.4 T where the  $E \times B$  effects are the largest.

### 13. Discussion and further improvements

A brief discussion of the obtained results is presented below.

The ERAM "charge spreading" effect has a small impact on the resolution of the measurement of the  $dE/dx$ . In this approach, when adding up the charges "shared" between pads due to the diffusion, the "charge spreading"

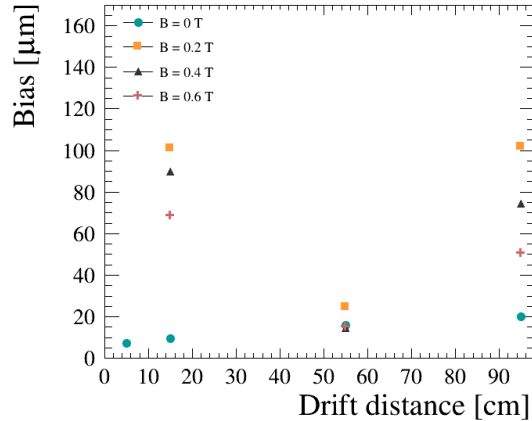


Figure 32: Track position bias with respect to the drift distance for the beam parallel to the pad side for different magnetic fields with a drift velocity of  $78.7 \text{ mm}/\mu\text{s}$  and peaking times of 200 ns.

time-dependent effect has to be taken into account not to bias the  $dE/dx$  measurement.

In contrast, the ERAM "charge spreading" effect allows for a dramatic improvement of spatial resolution. As shown in Sect. 11, if the maximal amplitude of the waveform is used, the spatial resolution does not depend significantly on the ERAM RC value. In fact one can calculate that for a point-like deposited charge the ratio of the maximal amplitude of a neighbour pad to the one of the leading pad, before convoluting with the electronics response, is independent of RC. But the shape of the charge signal as a function of time depends on RC and the integration of the electronics response will induce some dependence of this ratio on RC.

The spatial resolution also depends on the relative gain between neighbouring pads. This gain and its variation from pad to pad need to be well-measured and calibrated.

That is why measurements of RC and gain maps of the ERAM modules are performed using a point-like iron X-ray source placed close to the ERAM. These measurements are complementary to the test beams data analyses and will be a subject of a future publication.

The simulation allows to understand deeper the data from the test beam, and to disentangle different effects, when associated to the simpler data from the X-ray surveys.

## 14. Conclusions

In this paper we present the performances of the prototype of the HA-TPCs for the T2K Near Detector upgrade obtained during a test beam at DESY performed in 2021. The TPC was instrumented with one of the ERAM detectors that will be installed in the HA-TPCs and the final HA-TPC read-out electronics chain.

The test beam data allowed spatial and  $dE/dx$  resolutions to be determined as a function of the angle of the track with respect to the ERAM plane for all the drift distances of interest for T2K. Spatial resolution better than  $800\ \mu\text{m}$  is obtained for all the angles and all the drift distances using a dedicated clustering algorithm which is adapted to the track angle. Deposited energy resolution better than 10% is obtained for all the angles.

The data are compared with a simulation of the ERAM response, including the features of the resistive layer. As shown in this paper, the simulation is able to satisfactorily reproduce the observed charge sharing between neighboring pads. Spatial resolution and  $dE/dx$  resolution are also in good agreement between data and simulation.

## Acknowledgements

The measurements leading to these results have been performed at the Test Beam Facility at DESY Hamburg (Germany), a member of the Helmholtz Association. The authors would like to thank the technical team at the DESY II accelerator and test beam facility for the smooth operation of the test beam and the support during the test beam campaign.

We acknowledge the support of CEA and CNRS/IN2P3, France; DFG, Germany; INFN, Italy; National Science Centre (NCN) and Ministry of Science and Higher Education (Grant No. DIR/WK/2017/05), Poland; the Spanish Ministerio de Economía y Competitividad (SEIDI - MINECO) under Grant No. PID2019-107564GB-I00 (IFAE, Spain). IFAE is partially funded by the CERCA program of the Generalitat de Catalunya.

In addition, the participation of individual researchers and institutions has been further supported by H2020 Grant No. RISE-GA822070-JENNIFER2 2020, MSCA-COFUND-2016 No.754496, ANR-19-CE31-0001, RFBR grants #19-32-90100, the Secretariat for Universities and Research of the Ministry of Business and Knowledge of the Government of Catalonia and the European Social Fund (2022FLB 00336) and from the program Plan de Doctora-

dos Industriales of the Research and Universities Department of the Catalan Government (2022 DI 011).

## References

- [1] K. Abe, et al., The T2K Experiment, Nucl. Instrum. Meth. A659 (2011) 106–135. [arXiv:1106.1238](#), [doi:10.1016/j.nima.2011.06.067](#).
- [2] K. Abe, et al., Observation of Electron Neutrino Appearance in a Muon Neutrino Beam, Phys. Rev. Lett. 112 (2014) 061802. [arXiv:1311.4750](#), [doi:10.1103/PhysRevLett.112.061802](#).
- [3] K. Abe, et al., Constraint on the matter–antimatter symmetry-violating phase in neutrino oscillations, Nature 580 (7803) (2020) 339–344, [Erratum: Nature 583, E16 (2020)]. [arXiv:1910.03887](#), [doi:10.1038/s41586-020-2177-0](#).
- [4] K. Abe, et al., J-PARC Neutrino Beamline Upgrade Technical Design Report (8 2019). [arXiv:1908.05141](#).
- [5] K. Abe, et al., T2K ND280 Upgrade - Technical Design Report (1 2019). [arXiv:1901.03750](#).
- [6] P. A. Amaudruz, et al., The T2K Fine-Grained Detectors, Nucl. Instrum. Meth. A 696 (2012) 1–31. [arXiv:1204.3666](#), [doi:10.1016/j.nima.2012.08.020](#).
- [7] N. Abgrall, et al., Time Projection Chambers for the T2K Near Detectors, Nucl. Instrum. Meth. A 637 (2011) 25–46. [arXiv:1012.0865](#), [doi:10.1016/j.nima.2011.02.036](#).
- [8] I. Giomataris, R. De Oliveira, S. Andriamonje, S. Aune, G. Charpak, P. Colas, A. Giganon, P. Rebourgeard, P. Salin, Micromegas in a bulk, Nucl. Instrum. Meth. A560 (2006) 405–408. [arXiv:physics/0501003](#), [doi:10.1016/j.nima.2005.12.222](#).
- [9] K. Abe, et al., Improved constraints on neutrino mixing from the T2K experiment with  $3.13 \times 10^{21}$  protons on target, Phys. Rev. D 103 (11) (2021) 112008. [arXiv:2101.03779](#), [doi:10.1103/PhysRevD.103.112008](#).

- [10] K. Abe, et al., T2K ND280 Upgrade - Technical Design Report (2019). [arXiv:1901.03750](https://arxiv.org/abs/1901.03750).
- [11] S. Dolan, et al., Sensitivity of the upgraded T2K Near Detector to constrain neutrino and antineutrino interactions with no mesons in the final state by exploiting nucleon-lepton correlations, *Phys. Rev. D* 105 (3) (2022) 032010. [arXiv:2108.11779](https://arxiv.org/abs/2108.11779), [doi:10.1103/PhysRevD.105.032010](https://doi.org/10.1103/PhysRevD.105.032010).
- [12] A. Blondel, et al., The SuperFGD Prototype Charged Particle Beam Tests, *JINST* 15 (12) (2020) P12003. [arXiv:2008.08861](https://arxiv.org/abs/2008.08861), [doi:10.1088/1748-0221/15/12/P12003](https://doi.org/10.1088/1748-0221/15/12/P12003).
- [13] A. Korzenev, et al., A  $4\pi$  time-of-flight detector for the ND280/T2K upgrade, *JINST* 17 (01) (2022) P01016. [arXiv:2109.03078](https://arxiv.org/abs/2109.03078), [doi:10.1088/1748-0221/17/01/P01016](https://doi.org/10.1088/1748-0221/17/01/P01016).
- [14] P. Baron, D. Calvet, E. Delagnes, X. de la Broise, A. Delbart, F. Druilole, E. Monmarthe, E. Mazzucato, F. Pierre, M. Zito, AFTER, an ASIC for the readout of the large T2K time projection chambers, *IEEE Trans. Nucl. Sci.* 55 (2008) 1744–1752. [doi:10.1109/TNS.2008.924067](https://doi.org/10.1109/TNS.2008.924067).
- [15] D. Calvet, Back-End Electronics Based on an Asymmetric Network for Low Background and Medium- Scale Physics Experiments, *IEEE Trans. Nucl. Sci.* 66 (7) (2018) 998–1006. [arXiv:1806.07618](https://arxiv.org/abs/1806.07618), [doi:10.1109/TNS.2018.2884617](https://doi.org/10.1109/TNS.2018.2884617).
- [16] MIDAS – modern data acquisition system (2020).  
URL <https://midas.triumf.ca/>
- [17] R. Diener, et al., The DESY II Test Beam Facility, *Nucl. Instrum. Meth. A* 922 (2019) 265–286. [arXiv:1807.09328](https://arxiv.org/abs/1807.09328), [doi:10.1016/j.nima.2018.11.133](https://doi.org/10.1016/j.nima.2018.11.133).
- [18] D. Attié, et al., Characterization of resistive Micromegas detectors for the upgrade of the T2K Near Detector Time Projection Chambers, *Nucl. Instrum. Meth. A* 1025 (2022) 166109. [arXiv:2106.12634](https://arxiv.org/abs/2106.12634), [doi:10.1016/j.nima.2021.166109](https://doi.org/10.1016/j.nima.2021.166109).
- [19] D. Attié, et al., Performances of a resistive Micromegas module for the Time Projection Chambers of the T2K Near Detector upgrade,

- Nucl. Instrum. Meth. A 957 (2020) 163286. [arXiv:1907.07060](#), [doi:10.1016/j.nima.2019.163286](#).
- [20] D. Attie, Beam tests of Micromegas LC-TPC large prototype, JINST 6 (2011) C01007. [doi:10.1088/1748-0221/6/01/C01007](#).
- [21] OUESTRONIC company, <https://www.ouestronic.fr/> (2022).
- [22] S. Agostinelli, et al., GEANT4—a simulation toolkit, Nucl. Instrum. Meth. A 506 (2003) 250–303. [doi:10.1016/S0168-9002\(03\)01368-8](#).
- [23] J. Apostolakis, S. Giani, L. Urban, M. Maire, A. V. Bagulya, V. M. Grichine, An implementation of ionisation energy loss in very thin absorbers for the geant4 simulation package, Nuclear Instruments and Methods in Physics Research Section A: Accelerators, Spectrometers, Detectors and Associated Equipment 453 (2000) 597–605. [doi:10.1016/S0168-9002\(00\)00457-5](#).
- [24] N. Abgrall, et al., Time Projection Chambers for the T2K Near Detectors, Nucl. Instrum. Meth. A637 (2011) 25–46. [arXiv:1012.0865](#), [doi:10.1016/j.nima.2011.02.036](#).
- [25] M. S. Dixit, A. Rankin, Simulating the charge dispersion phenomena in micro pattern gas detectors with a resistive anode, Nucl. Instrum. Meth. A566 (2006) 281–285. [arXiv:physics/0605121](#), [doi:10.1016/j.nima.2006.06.050](#).
- [26] M. Ester, H.-P. Kriegel, J. Sander, X. Xu, A density-based algorithm for discovering clusters in large spatial databases with noise, in: Proceedings of the Second International Conference on Knowledge Discovery and Data Mining, AAAI Press, 1996, pp. 226–231.
- [27] R. Gluckstern, Uncertainties in track momentum and direction, due to multiple scattering and measurement errors, Nuclear Instruments and Methods 24 (1963) 381–389. [doi:https://doi.org/10.1016/0029-554X\(63\)90347-1](#).  
URL <https://www.sciencedirect.com/science/article/pii/S0029554X63903471>
- [28] K. Boudjemline, M. S. Dixit, J. P. Martin, K. Sachs, Spatial resolution of a GEM readout TPC using the charge dispersion signal, Nucl. Instrum.

- Meth. A574 (2007) 22–27. [arXiv:physics/0610232](https://arxiv.org/abs/physics/0610232), [doi:10.1016/j.nima.2007.01.017](https://doi.org/10.1016/j.nima.2007.01.017).
- [29] P. Colas, First test results from a Micromegas large TPC prototype, Nucl. Instrum. Meth. A623 (2010) 100–101. [doi:10.1016/j.nima.2010.02.161](https://doi.org/10.1016/j.nima.2010.02.161).
- [30] A. Bellerive, K. Boudjemline, R. Carnegie, M. Dixit, J. Miyamoto, E. Neuheimer, A. Rankin, E. Rollin, K. Sachs, J. P. Martin, V. Lepeltier, P. Colas, A. Giganon, I. Giomataris, Spatial resolution of a micromegas-tpc using the charge dispersion signal (2005). [doi:10.48550/ARXIV.PHYSICS/0510085](https://doi.org/10.48550/ARXIV.PHYSICS/0510085).  
URL <https://arxiv.org/abs/physics/0510085>
- [31] <https://garfield.web.cern.ch/garfield> (2010).
- [32] C. Greife, Magnetic field map for a large tpc prototype (2008).